




Diffuse interface model for a single-component liquid-vapor systemTao Chen ^{1,*}, Chunhua Zhang ², and Lian-Ping Wang ¹¹*Department of Mechanics and Aerospace Engineering, Southern University of Science and Technology, Shenzhen 518055, China*²*School of Energy and Power Engineering, North University of China, Taiyuan 030051, China*

(Received 28 August 2022; revised 26 November 2022; accepted 25 January 2023; published 17 February 2023)

We elucidate the theoretical relationships among fundamental physical concepts that are involved in the diffuse interface modeling for an isothermal single-component liquid-vapor system, which cover both the equation of state (EOS) and the surface tension force. As an example, a flat surface at equilibrium is discussed both theoretically and numerically by using two different approaches. Particularly, the force structure in the transition region is clearly presented, which demonstrates that the capillary contributions due to the density gradients can suppress the mechanical instability of the thermodynamic pressure and lead to constant hydrodynamic pressure (and chemical potential). Then, by comparing with the van der Waals (vdW) EOS for a flat interface at equilibrium, it is shown that applying the double-well approximation can give qualitative predictions for relatively high density ratio ($\rho_l/\rho_g = 7.784$) and satisfactory results for relatively low density ratio ($\rho_l/\rho_g = 1.774$). The main cause for this observation is attributed to the nonlinear variation of the generalized coefficient function in the double-well formulation at different density ratios. In addition, for the latter case, we simulate a droplet impact on a hydrophilic wall by using a recently proposed well-balanced discrete unified gas kinetic scheme (WB-DUGKS), which justifies the applicability of the double-well approximation to complex interfacial dynamics in the low-density-ratio limit. Furthermore, the reason for the inconsistency between the coefficients of the mean-field force expressions in the existing literature is explained.

DOI: [10.1103/PhysRevE.107.025104](https://doi.org/10.1103/PhysRevE.107.025104)**I. INTRODUCTION**

Physical modeling on the interface between two fluids has been widely discussed from different perspectives [1–9]. The sharp interface model considers two fluids separated by an interface with zero thickness which needs to be tracked explicitly in the numerical simulation. Both fluids satisfy the Navier-Stokes (NS) equations, which are properly coupled by virtue of the interfacial boundary conditions. The interface is equipped with some fundamental physical properties such as the surface tension, and the physical quantities are allowed to have a jump across the interface [3]. In contrast, the interface exhibits a finite thickness from the diffuse-interface perspective, where the physical quantities vary smoothly in the transition region between the bulk phases [4,7,10]. Two fluids are described by one set of Navier-Stokes-Korteweg (NSK) equations. Therefore, explicit tracking of the interface is circumvented in the diffuse interface model.

Various diffuse interface models have been successfully applied to investigate fluid hydrodynamics and a wide range of interfacial phenomena [4,7,11,12]. It has been recognized that the diffuse interface model is particularly suitable for near-critical liquid-vapor flows (small density ratio), complex topological changes and large deformations of the interface, interface breakup and coalescence, and so on, where the traditional sharp interface model may fail to give accurate prediction of the interfacial changes. In recent years, some new numerical schemes and methods were proposed and

applied to simulate different kinds of complex interfacial flows based on the diffuse interface model [10,11,13–22]. To our knowledge, most of the existing methods cannot give accurate predictions for the interfacial structure under a specific equation of state (EOS). The sharp interface methods do not provide any opportunity to study the interfacial structure, where only the total jump of a physical quantity across the interface can be extracted. The numerical studies based on the phase field method usually have some artificial numerical treatments in the interfacial region to maintain the mass flux and the hyperbolic tangent profile. Moreover, the spurious velocity and the spurious chemical potential inherently exist in the traditional lattice Boltzmann method (LBM) due to the discretization errors in the force term [10]. Compared to these existing methods, the recently developed well-balanced discrete unified gas kinetic scheme (WB-DUGKS) [10,23,24] can remove the spurious currents thoroughly, making it possible to discuss the interfacial structure.

This paper attempts to elucidate the theoretical relationships among the fundamental physical concepts involved in the diffuse interface modeling for an isothermal single-component liquid-vapor system. A general description is provided before subsequent detailed discussions invoking specific model approximations. First, in Secs. II and III, under the Helmholtz-free-energy-based variational description, relationships among different forms of the chemical potential gradient force are clarified. Second, in Sec. IV, we provide two different but equivalent approaches to investigate a flat interface at equilibrium, from which a deeper understanding of the force structure of the transition region is obtained. Third, in Sec. V, we discuss the EOS and its double-well

*Corresponding author: 1601111553@pku.edu.cn

approximation, followed by detailed comparison of their predictions concerning the interfacial structures for the flat interface problem (Sec. VI).

Furthermore, in order to justify the applicability of the double-well approximation to complex interfacial flows for near-critical fluids, we simulate a droplet impact on a hydrophilic wall using the well-balanced discrete unified gas kinetic scheme (WB-DUGKS), as shown in Sec. VII. It is noted that the pressure drop in the EOS is directly related to the mean field force, which also includes the surface tension effect. In Sec. VIII, we explain the reason for the inconsistency between the coefficients of the mean-field force expressions in the existing literature, which is important for understanding the physical modeling of the interfacial force. Conclusions are given in Sec. IX. Appendix A documents the validation of the developed WB-DUGKS code by comparing with the analytical solution. The L_2 errors between the analytical and approximate solutions are discussed in Appendix B. In Appendix C, an extended discussion on the speed of sound and interfacial compressibility is provided.

II. FREE ENERGY, CHEMICAL POTENTIAL, AND EQUATION OF STATE

The thermodynamics of an isothermal single-component liquid-vapor system at equilibrium can be described by the classical second-gradient theory, where the corresponding Helmholtz free energy functional is given by [1,2,14,25]

$$\mathcal{F}(\rho, \nabla\rho) = \int_V \left(\psi(\rho) + \frac{1}{2}\kappa\|\nabla\rho\|^2 \right) dV, \quad (1)$$

where ρ is the fluid density, κ is a constant interfacial free energy coefficient partially governing the surface tension σ_s , and V is the integral volume occupied by the fluids. The first term $\psi(\rho)$ is the bulk free energy density while the second term $\kappa\|\nabla\rho\|^2/2$ is the interfacial free energy density caused by the nonlocal molecular interactions. The total free energy density f is the sum of these two contributions, i.e., $f \equiv \psi(\rho) + \kappa\|\nabla\rho\|^2/2$.

The first-order variation of the free energy functional with respect to the density gives the chemical potential μ_ρ , namely,

$$\mu_\rho \equiv \frac{\delta\mathcal{F}}{\delta\rho} = \mu_0 - \kappa\nabla^2\rho, \quad (2)$$

where the first term is the bulk chemical potential $\mu_0 \equiv \partial_\rho\psi$ and the second term is determined by the capillary contribution due to the Laplacian of density. When the bulk free energy density $\psi(\rho)$ is given, the thermodynamic pressure p_0 (namely, the EOS) is evaluated by the following expression:

$$p_0 = \rho\mu_0 - \psi. \quad (3)$$

By applying the spatial gradient operator ∇ on both sides of Eq. (3), a thermodynamic identity is readily obtained as

$$\rho\nabla\mu_0 = \nabla p_0, \quad (4)$$

which indicates that the gradient of the thermodynamic pressure ∇p_0 is proportional to that of the bulk chemical potential $\nabla\mu_0$. Since p_0 and μ_0 are functions of the density ρ , we can also write Eq. (4) as $\partial_\rho p_0 = \rho\partial_\rho\mu_0 = \rho\partial_\rho\partial_\rho\psi$, which is exactly the same as the result by Jamet *et al.* [7]. However, the

essential link between different equations was not provided in their paper, where they actually gave an extended description based on the earlier work of Rowlinson and Widom [25].

III. HYDRODYNAMICS: NAVIER-STOKES-KORTEWEG EQUATIONS

The hydrodynamics of an isothermal two-phase flow system can be well described by the Navier-Stokes-Korteweg (NSK) equations:

$$\frac{\partial\rho}{\partial t} + \nabla \cdot (\rho\mathbf{u}) = 0, \quad (5a)$$

$$\frac{\partial(\rho\mathbf{u})}{\partial t} + \nabla \cdot (\rho\mathbf{u}\mathbf{u}) = -\rho\nabla\mu_\rho + \nabla \cdot \mathbf{\Pi} + \rho\mathbf{G}, \quad (5b)$$

where \mathbf{u} is the macroscopic velocity and $-\rho\nabla\mu_\rho$ is the chemical potential gradient force (potential form) [10,26]. $\mathbf{\Pi} \equiv 2\mu\mathbf{S} + \lambda\vartheta\mathbf{I}$ is the viscous stress tensor, where μ is the dynamic viscosity and $\lambda = \mu_V - 2\mu/3$ with μ_V being the bulk viscosity. \mathbf{G} is the acceleration due to the external force.

We point out that two equivalent expressions of the chemical potential gradient force can be readily obtained by virtue of only two identities. First, by using the thermodynamic identity in Eq. (4), an equivalent pressure form of the chemical potential gradient force is obtained as [27]

$$-\rho\nabla\mu_\rho = -\nabla p_0 + \kappa\rho\nabla\nabla^2\rho. \quad (6)$$

Then, by virtue of the identity

$$\rho\nabla\nabla^2\rho = \nabla \cdot [(\rho\nabla^2\rho + \frac{1}{2}\|\nabla\rho\|^2)\mathbf{I} - \nabla\rho\nabla\rho], \quad (7)$$

the chemical potential gradient force can be written in a divergence form,

$$-\rho\nabla\mu_\rho = -\nabla \cdot \mathbf{P}, \quad (8)$$

where the Korteweg pressure tensor \mathbf{P} is given by [28]

$$\begin{aligned} \mathbf{P} &= (p_0 - \kappa\rho\nabla^2\rho - \frac{1}{2}\kappa\|\nabla\rho\|^2)\mathbf{I} + \kappa\nabla\rho\nabla\rho \\ &\equiv p\mathbf{I} + \kappa\nabla\rho\nabla\rho. \end{aligned} \quad (9)$$

Equation (8) provides two different ways to express the physical origin of the rate of change of the fluid momentum. On the one hand, as indicated by its left-hand side, the two-phase flow system is driven by the chemical potential gradient to transport the fluid momentum, so that the phase equilibrium can be reached with the minimum free energy. On the other hand, its physical effect can be described as the divergence of the second-order tensor \mathbf{P} (like that of the viscous stress tensor $\mathbf{\Pi}$ accounting for the viscous stress), which yields an additional force on a fluid element. In Eq. (9), the nonlocal total pressure p is defined as

$$p \equiv p_0 - \kappa\rho\nabla^2\rho - \frac{1}{2}\kappa\|\nabla\rho\|^2, \quad (10)$$

which includes the thermodynamic pressure p_0 and two capillary contributions due to the density gradients.

By using Eqs. (2) and (3), it follows that

$$p = \rho\mu_\rho - f, \quad (11)$$

which directly relates the total pressure p to the chemical potential μ_ρ and the free energy density f . Note that Eq. (9) is formally consistent with the pressure tensor derived from the

kinetic Enskog-Vlasov (E-V) equation, which combines Enskog's kinetic theory for short-range molecular interaction due to the repulsive force [29] and the mean field theory [28,30] for long-range attractive interaction between molecules.

Furthermore, we relate Eq. (9) to an equivalent stress form of the Korteweg pressure tensor \mathbf{P} reported by Lee and Lin [31]. Using the notations in this paper, it can be easily derived by adjusting the terms in Eq. (9), which results in

$$\mathbf{P} = p_h \mathbf{I} - \Phi, \quad (12a)$$

with p_h and Φ given by

$$p_h \equiv p_0 - \kappa \rho \nabla^2 \rho + \frac{1}{2} \kappa \|\nabla \rho\|^2, \quad (12b)$$

$$\Phi \equiv \kappa (\|\nabla \rho\|^2 \mathbf{I} - \nabla \rho \nabla \rho), \quad (12c)$$

where p_h is defined as the hydrodynamic pressure and Φ is the surface tension stress tensor. The hydrodynamic pressure p_h is typically of the order $\mathcal{O}(\text{Ma}^2)$, which varies smoothly across the interfacial region compared to that of the thermodynamic pressure p_0 . Here, Ma is the characteristic Mach number. Φ has three eigenvalues (λ_1 , λ_2 , and λ_3) and three mutually perpendicular principal axes. One of the principal axes is parallel to the unit normal vector of the density isosurface S , namely, $\mathbf{n} = \nabla \rho / \|\nabla \rho\|$, whose corresponding eigenvalue is $\lambda_1 = 0$. The two remaining eigenvalues are equal to twice the interfacial energy density (i.e., $\lambda_2 = \lambda_3 = \kappa \|\nabla \rho\|^2$), whose corresponding principal axes can be specified as any two perpendicular vectors lying in the tangent plane of S . The integral of λ_2 (or λ_3) gives the surface tension coefficient $\sigma_s = \kappa \int_{-\infty}^{+\infty} (\frac{d\rho}{d\zeta})^2 d\zeta$, where ζ is the surface-normal coordinate. The surface tension contains the contributions from both the bulk and interfacial gradient energies [7,25]. We think that Eq. (12a) gives a very neat separation of hydrodynamic pressure p_h and the surface tension force σ_s .

IV. FLAT INTERFACE PROBLEM

The simplest case for two-phase flow is a flat diffuse interface at equilibrium, which is essentially one-dimensional (1D) and can be solved directly. Although it is geometrically simple, a better understanding of the interfacial structure between the saturated phases can be achieved by studying the problem from two different perspectives (namely, the chemical equilibrium and the force balance). In this section, we provide two approaches to derive the various forms of the balance equation at equilibrium, where the relations among the fundamental concepts are clearly presented. In particular, the well-known Maxwell equal-area rule (namely, Maxwell construction) is recovered as a corollary. The equivalence between different approaches is strictly proved. A complete derivation that naturally combines different concepts cannot be found in the existing literature. The derivation in this section is more direct and systematic, which makes the necessary preparation for the comparisons in Section V and VI.

A. Approach A: Chemical equilibrium

Consider a flat interface at equilibrium which separates the liquid and gas phases with their saturated densities ρ_l and ρ_g in the bulk regions [i.e., asymptotic boundary conditions $\rho(+\infty) = \rho_l$, $\rho(-\infty) = \rho_g$, and $d\rho/dx(x \rightarrow \pm\infty) = 0$ are

required for the transition region]. By minimizing the free energy functional $\mathcal{F}(\rho, \nabla \rho)$ or equivalently by setting the fluid velocity $\mathbf{u} = \mathbf{0}$ in the NSK equations [Eqs. (5a) and (5b)], one can obtain a constant chemical potential, i.e.,

$$\mu_\rho = \mu_0 - \kappa \frac{d^2 \rho}{dx^2} = \mu^*, \quad (13)$$

where x is the surface normal coordinate satisfying $\rho(x = 0) = (\rho_l + \rho_g)/2$, and $\mu^* = \mu_0(\rho_l) = \mu_0(\rho_g)$ represents a constant chemical potential, which is a combination of the bulk chemical potential and the contribution from the Laplacian of density.

Since the density $\rho(x)$ has a one-to-one mapping with respect to the coordinate x in the transition region, we can reduce the order of the derivative via the transformation

$$\frac{d^2 \rho}{dx^2} = \frac{d\rho}{dx} \frac{d}{d\rho} \left(\frac{d\rho}{dx} \right) = \frac{d}{d\rho} \left[\frac{1}{2} \left(\frac{d\rho}{dx} \right)^2 \right]. \quad (14)$$

From Eqs. (13) and (14), we obtain

$$\frac{d}{d\rho} \left[\psi - \frac{1}{2} \kappa \left(\frac{d\rho}{dx} \right)^2 \right] = \mu^*, \quad (15)$$

which results in the following energy balance equation:

$$\frac{1}{2} \kappa \left(\frac{d\rho}{dx} \right)^2 = \psi - \rho \mu^* + p^* \equiv \bar{\psi}(\rho), \quad (16)$$

where $p^* = p_0(\rho_l) = p_0(\rho_g)$ is the constant pressure in the bulk fluid regions and $\bar{\psi}(\rho)$ is the redefined (or effective) bulk free energy density. Equation (16) allows a smooth transition across the phase interface between the saturated bulk phases at equilibrium, and indicates that the interfacial free energy density is equal to the effective bulk free energy density at each spatial point. The saturated densities ρ_l and ρ_g can be obtained by solving the two algebraic equations $p_0(\rho_l) = p_0(\rho_g)$ and $\mu_0(\rho_l) = \mu_0(\rho_g)$ for two unknowns. Note that Eq. (16) is the same as Eq. (8) of Jamet *et al.* [7], where the derivation details were not provided. The key point addressed by them is different from the present paper. Their study actually provided an extended discussion on the modification of the EOS in order to simulate liquid-vapor flow with phase change.

By using Eq. (3), Eq. (16) can be equivalently written as

$$\frac{1}{2} \kappa \left(\frac{d\rho}{dx} \right)^2 = \psi(\rho) - \psi(\rho_g) - \mu_0(\rho_g)(\rho - \rho_g) \quad (17a)$$

or

$$\frac{1}{2} \kappa \left(\frac{d\rho}{dx} \right)^2 = \psi(\rho) - \psi(\rho_l) - \mu_0(\rho_l)(\rho - \rho_l). \quad (17b)$$

Eqs. (17a) and (17b) imply that the bulk free energy densities are related by

$$\psi(\rho_l) = \psi(\rho_g) + \mu^*(\rho_l - \rho_g) \Leftrightarrow p^* = p_0(\rho_l) = p_0(\rho_g). \quad (18)$$

In terms of the effective bulk free energy density $\bar{\psi}(\rho)$ in Eq. (16), we can redefine the thermodynamic pressure \bar{p}_0 and the bulk chemical potential $\bar{\mu}_0$ as

$$\bar{\mu}_0 \equiv \frac{\partial \bar{\psi}}{\partial \rho} \quad \text{and} \quad \bar{p}_0 \equiv \rho \frac{\partial \bar{\psi}}{\partial \rho} - \bar{\psi}. \quad (19)$$

Then, it can be proved that

$$\bar{\mu}_0 = \mu_0 - \mu^*, \quad \bar{p}_0 = p_0 - p^*. \quad (20)$$

Equations (20) shows that \bar{p}_0 (or $\bar{\mu}_0$) only differs from p_0 (or μ_0) by a constant. In other words, at equilibrium, we have $\bar{\mu}_0 = 0$ and $\bar{p}_0 = 0$ in the bulk regions.

B. Approach B: Force balance

Equations (8) and (9) give a description of the phase equilibrium through the divergence of the Korteweg pressure tensor \mathbf{P} . For 1D case, using Eq. (12), the surface tension stress tensor Φ vanishes so that $\mathbf{P} = p_h \mathbf{I}$ and $\nabla \cdot \mathbf{P} = \nabla p_h$, which gives

$$\frac{d}{dx} \left[p_0 - \kappa \rho \frac{d^2 \rho}{dx^2} + \frac{1}{2} \kappa \left(\frac{d\rho}{dx} \right)^2 \right] = 0, \quad (21)$$

whose first integral is expressed as

$$p_0 - \kappa \rho \frac{d^2 \rho}{dx^2} + \frac{1}{2} \kappa \left(\frac{d\rho}{dx} \right)^2 = p^*. \quad (22)$$

The left-hand side of Eq. (22) is just the hydrodynamic pressure p_h introduced in Eq. (12b), which varies smoothly across the interfacial region compared to the thermodynamic pressure p_0 . At equilibrium, Eq. (22) actually implies a constant hydrodynamic pressure $p_h = p^*$ in the whole domain.

It is noted that the capillary stresses in Eq. (22) can be written as

$$-\kappa \rho \frac{d^2 \rho}{dx^2} + \frac{1}{2} \kappa \left(\frac{d\rho}{dx} \right)^2 = -\kappa \rho^2 \left[\frac{1}{\rho} \frac{d^2 \rho}{dx^2} - \frac{1}{\rho^2} \frac{1}{2} \left(\frac{d\rho}{dx} \right)^2 \right]. \quad (23)$$

Using Eq. (14) to replace $d^2 \rho / dx^2$ in the right-hand side of Eq. (23) and applying the chain rule for the partial derivative, we obtain

$$-\kappa \rho \frac{d^2 \rho}{dx^2} + \frac{1}{2} \kappa \left(\frac{d\rho}{dx} \right)^2 = -\frac{1}{2} \kappa \rho^2 \frac{d}{d\rho} \left[\frac{1}{\rho} \left(\frac{d\rho}{dx} \right)^2 \right]. \quad (24)$$

Therefore, Eq. (22) is transformed into

$$p_0 - \frac{1}{2} \kappa \rho^2 \frac{d}{d\rho} \left[\frac{1}{\rho} \left(\frac{d\rho}{dx} \right)^2 \right] = p^*, \quad (25)$$

which can be further written as

$$d \left[\frac{1}{\rho} \frac{1}{2} \kappa \left(\frac{d\rho}{dx} \right)^2 \right] = (p^* - p_0) d \left(\frac{1}{\rho} \right). \quad (26)$$

Integrating both sides of Eq. (26) from ρ_l to ρ , we obtain the following representation:

$$\frac{1}{2} \kappa \left(\frac{d\rho}{dx} \right)^2 = \rho \int_{\rho_l}^{\rho} (p^* - p_0) d \left(\frac{1}{\rho} \right). \quad (27)$$

If the upper limit of the integral is taken as the inverse of the saturated fluid density ρ_g^{-1} , the well-known Maxwell equal-area rule is naturally recovered, namely,

$$\int_{\rho_l}^{\rho_g^{-1}} p_0 d \left(\frac{1}{\rho} \right) = p^* \left(\frac{1}{\rho_g} - \frac{1}{\rho_l} \right). \quad (28)$$

With Eq. (28), it is clear that the lower limit of the right-hand side of Eq. (27) can be replaced by ρ_g^{-1} without changing the integral value.

C. Equivalence between Eqs. (16) and (27)

Now we can prove the equivalence of Eqs. (16) and (27).

First, we note that the thermodynamic pressure p_0 in Eq. (16) can be rewritten as

$$p_0 = \rho^2 \left(\frac{1}{\rho} \frac{d\psi}{d\rho} - \frac{1}{\rho^2} \psi \right) = \rho^2 \frac{d}{d\rho} \left(\frac{\psi}{\rho} \right), \quad (29)$$

which is equivalent to

$$-p_0 d \left(\frac{1}{\rho} \right) = d \left(\frac{\psi}{\rho} \right). \quad (30)$$

Second, integrating Eq. (30) from ρ_l to ρ , we obtain

$$-\int_{\rho_l}^{\rho} p_0 d \left(\frac{1}{\rho} \right) = \frac{\psi}{\rho} - \frac{\psi(\rho_l)}{\rho_l}. \quad (31)$$

In addition, the following integral is always valid due to constant p^* , i.e.,

$$\int_{\rho_l}^{\rho} p^* d \left(\frac{1}{\rho} \right) = p^* \left(\frac{1}{\rho} - \frac{1}{\rho_l} \right). \quad (32)$$

Therefore, the right-hand side of Eq. (27) can be evaluated by the sum of Eqs. (31) and (32):

$$\rho \int_{\rho_l}^{\rho} (p^* - p_0) d \left(\frac{1}{\rho} \right) = \psi(\rho) - \frac{\psi(\rho_l) + p^*}{\rho_l} \rho + p^*. \quad (33)$$

Finally, by using $p^* = \rho_l \mu^* - \psi(\rho_l)$, the coefficient of the second term in the right-hand side of Eq. (33) is simplified as $-\psi(\rho_l) + p^* / \rho_l = -\mu^*$. Therefore, the equivalence between Eqs. (16) and (27) is proved.

D. Force structure in the transition region between two phases at equilibrium

As an example, we consider the van der Waals (vdW) EOS: [25]

$$p_0 = \frac{\rho RT}{1 - b\rho} - a\rho^2, \quad (34)$$

where a is a parameter due to the attractive molecular interaction, b accounts for the volume correction due to the finite molecular size effect, and R is the gas constant. By solving the equations $\partial_\rho p_0(\rho_c, T_c) = 0$ and $\partial_\rho \partial_\rho p_0(\rho_c, T_c) = 0$ at the critical point, the critical density ρ_c , temperature T_c , and pressure p_c of Eq. (34) are obtained as

$$\rho_c = \frac{1}{3b}, \quad T_c = \frac{8a}{27Rb}, \quad p_c = \frac{a}{27b^2}. \quad (35)$$

The corresponding bulk free energy density $\psi(\rho)$ is

$$\psi(\rho) = \rho RT \ln \left(\frac{b\rho}{1 - b\rho} \right) - a\rho^2. \quad (36)$$

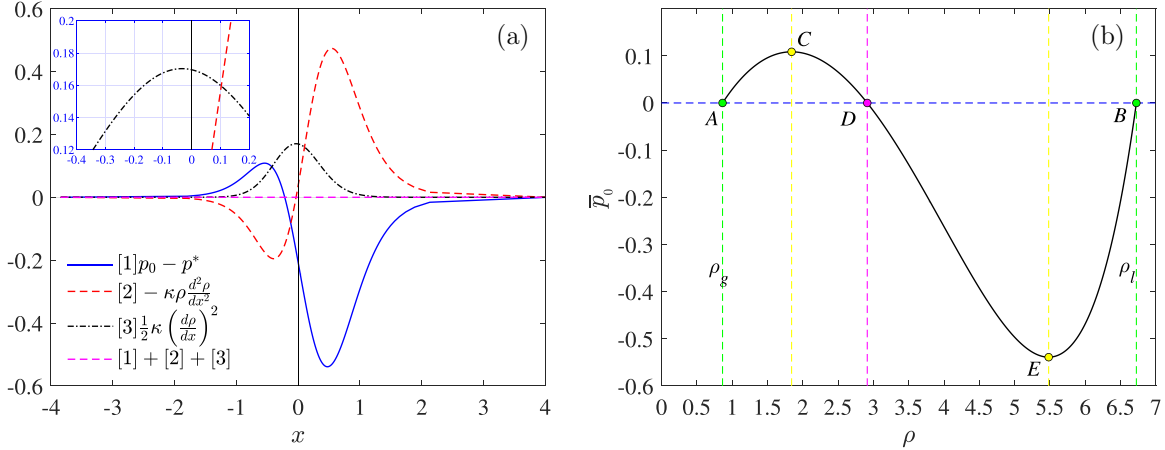


FIG. 1. (a) Distributions of the thermodynamic pressure $\bar{p}_0 = p_0 - p^*$ and two capillary stresses $[-\kappa\rho d^2\rho/dx^2$ and $\kappa(d\rho/dx)^2/2$] in the transition region for a flat interface at equilibrium. (b) $\bar{p}_0 - \rho$ diagram. Three zero-crossing points (A , B , and D) and two extreme points (C and E) are marked. CE represents the unstable region of the thermodynamic pressure. A and B correspond to the saturated bulk densities with the same thermodynamic pressure.

In addition, the bulk chemical potential $\mu_0(\rho)$ is

$$\mu_0(\rho) = RT \left[\ln \left(\frac{b\rho}{1-b\rho} \right) + \frac{1}{1-b\rho} \right] - 2a\rho. \quad (37)$$

For convenience, the comparison for the flat interface problem will be presented in the lattice units, which is widely used in the community of the LBM [24,32]. Here, we choose $a = 9/49$, $b = 2/21$ and $R = 1$. The corresponding critical values are $\rho_c = 3.500$, $T_c = 0.571$, and $p_c = 0.750$, respectively. The coexisting densities (ρ_l and ρ_g) and the bulk thermodynamic pressure p^* can be obtained through the Maxwell equal-area rule [see Eq. (28)]. At the temperature $T = 0.46 < T_c$, the coexisting saturated densities are $\rho_l = 6.723$ and $\rho_g = 0.864$, which result in the density ratio $\rho_l/\rho_g = 7.784$. The bulk thermodynamic pressure and chemical potential are $p^* = 0.296$ and $\mu^* = -0.926$, respectively. The density profile $\rho(x)$ at equilibrium can be obtained by solving Eq. (16) numerically. The interfacial free energy coefficient κ is set as 0.02. Then, with the obtained density field $\rho(x)$, the first-order and the second-order derivatives of the density field ($d\rho/dx$ and $d^2\rho/dx^2$) can be obtained by using Eqs. (13) and (16).

Figure 1(a) shows the distributions of different terms in Eq. (22), which include the (redefined) thermodynamic pressure $\bar{p}_0 = p_0 - p^*$ and the capillary stresses caused by the density gradients $[-\kappa\rho d^2\rho/dx^2$ and $\kappa(d\rho/dx)^2/2$]. The sum of these three terms is equal to zero at equilibrium, which implies the consistency of the above analysis from different perspectives. The capillary stress $\kappa(d\rho/dx)^2/2$ is equal to the bulk chemical potential $\bar{\psi}$, which is not fully symmetric with respect to the origin $x = 0$ (as shown in the zoom-in view) due to different interaction strengths between the interfacial region and each bulk region. It is observed that there exists a portion of the blue curve with negative slope $d\bar{p}_0/dx < 0$. Since $d\rho/dx > 0$ holds at the same region, we have $d\bar{p}_0/d\rho < 0$, which implies that this region is mechanically unstable [as displayed in Fig. 1(b)]. Fortunately, the thermodynamic pressure $\bar{p}_0 = p_0 - p^*$ in the transition region is balanced by the capillary contributions due to the density gradients, finally

leading to the phase equilibrium (with constant hydrodynamic pressure).

We observe that the term $\kappa(d\rho/dx)^2/2$ remains non-negative in the whole region. In contrast, both \bar{p}_0 and $-\kappa\rho(d^2\rho/dx^2)$ have a zero-crossing point in this region (where $d\bar{p}_0/d\rho < 0$). It is noticed that these two zero-crossing points do not coincide with each other, which divides the unsteady portion into three parts. Before the first zero-crossing point, \bar{p}_0 is positive and $-\kappa\rho(d^2\rho/dx^2)$ is negative. $\kappa(d\rho/dx)^2/2$ tends to increase the magnitude of \bar{p}_0 , whose sum is suppressed by $-\kappa\rho(d^2\rho/dx^2)$. Between these two zero-crossing points, \bar{p}_0 becomes negative, which is enhanced by the capillary contribution $-\kappa\rho(d^2\rho/dx^2)$. The sum of these two terms is neutralized by $\kappa(d\rho/dx)^2/2$. After the second zero-crossing point, \bar{p}_0 decreases rapidly to reach a global negative valley point. It is clear that the positive contribution of $\kappa(d\rho/dx)^2/2$ itself cannot maintain the balance. However, the magnitude of $-\kappa\rho(d^2\rho/dx^2)$ grows rapidly to highly positive values, which leads to the global equilibrium.

V. THEORETICAL ANALYSIS ON DOUBLE-Well APPROXIMATION

For near-critical fluids (in a small vicinity of the critical point of the EOS), many studies [10,27,33] adopted the well-known double-well approximation for the bulk free energy density $\bar{\psi}(\rho)$, namely,

$$\bar{\psi}(\rho) \approx \beta_0(\rho - \rho_l)^2(\rho - \rho_g)^2, \quad (38)$$

where the positive coefficient β_0 is assumed to be a constant. In the original paper of Cahn and Hillard [34], β_0 is taken as

$$\beta_0 = \beta_{CH} \equiv \frac{1}{4!} \frac{\partial^4 \bar{\psi}}{\partial \rho^4}(\rho_c, T_c), \quad (39)$$

where ρ_c and T_c are the critical density and the critical temperature of a given EOS for p_0 , respectively. This is reasonable because both the second and third derivatives of $\bar{\psi}$ are equal to zero at the critical point.

The advantage for this simple representation is that the interfacial thickness parameter W and the surface tension coefficient σ_s can be tuned separately based on the corresponding analytical solution of a flat surface at equilibrium:

$$\rho(x) = \frac{\rho_l + \rho_g}{2} + \frac{\rho_l - \rho_g}{2} \tanh\left(\frac{2x}{W}\right). \quad (40)$$

which can be obtained by solving Eq. (16). In other words, they can be explicitly evaluated through the following relations [2,6,7]:

$$\begin{aligned} W &= \frac{1}{\rho_l - \rho_g} \sqrt{\frac{8\kappa}{\beta_0}}, \quad \sigma_s = \kappa \int_{-\infty}^{+\infty} \left(\frac{d\rho}{dx}\right)^2 dx \\ &= \frac{1}{6}(\rho_l - \rho_g)^3 \sqrt{2\kappa\beta_0}, \end{aligned} \quad (41)$$

when κ and β_0 are already given.

It is also noted that Eq. (38) has been widely applied in two-phase flow simulations focusing on phase separation, so it is not limited to single-component liquid-vapor flows. By introducing a flexible pressure parameter in the momentum equation to enhance the incompressibility [15,18,35], Eq. (38) has been generalized for the order parameter in the phase-field method to simulate large-density-ratio fluids when combining with the phase-field evolution equations [34,36]. However, for the original form in Eq. (38) corresponding to isothermal liquid-vapor flows, whether this simple approximation can match the given EOS is not fully explored even for relatively low density ratio ρ_l/ρ_g [for example, $\rho_l/\rho_g \lesssim \mathcal{O}(10)$].

Instead of adopting the double-well approximation with a constant coefficient β_0 , we prefer to discuss this problem in a more general way and assume the following form for $\bar{\psi}(\rho)$:

$$\bar{\psi}(\rho) = \beta(\rho)(\rho - \rho_l)^2(\rho - \rho_g)^2, \quad (42)$$

where $\beta(\rho)$ is a smooth function of the density to match the EOS for fixed temperature T . To distinguish Eq. (42) from the double-well *approximation* with the constant coefficient β_0 [see Eq. (38)], it is referred to as the double-well *formulation* with the density-dependent coefficient $\beta(\rho)$.

When $\rho \neq \rho_l$ and ρ_g , the coefficient function $\beta(\rho)$ can be directly evaluated by

$$\beta(\rho) = \frac{\bar{\psi}(\rho)}{(\rho - \rho_l)^2(\rho - \rho_g)^2}, \quad (43)$$

where $\bar{\psi}(\rho)$ is given by the considered EOS. When the density ρ is equal to ρ_l or ρ_g , the values of $\beta(\rho)$ at the saturated densities (ρ_l and ρ_g) can be obtained by virtue of the limit theory.

Since $\bar{\psi}(\rho_g) = 0$ and $\bar{\mu}_0(\rho_g) = \partial_\rho \bar{\psi}(\rho_g) = 0$, applying the l'Hôpital rule twice gives

$$\begin{aligned} \beta(\rho_g) &= \lim_{\rho \rightarrow \rho_g} \frac{\bar{\psi}(\rho)}{(\rho - \rho_l)^2(\rho - \rho_g)^2} \\ &= \lim_{\rho \rightarrow \rho_g} \frac{\bar{\mu}_0(\rho)}{2(\rho - \rho_g)(\rho - \rho_l)(2\rho - \rho_l - \rho_g)} \\ &= \frac{1}{2(\rho_l - \rho_g)^2} \frac{\partial^2 \bar{\psi}}{\partial \rho^2}(\rho_g). \end{aligned} \quad (44)$$

Similarly, due to $\bar{\psi}(\rho_l) = 0$ and $\bar{\mu}_0(\rho_l) = \partial_\rho \bar{\psi}(\rho_l) = 0$, $\beta(\rho_l)$ is obtained as

$$\beta(\rho_l) = \frac{1}{2(\rho_l - \rho_g)^2} \frac{\partial^2 \bar{\psi}}{\partial \rho^2}(\rho_l). \quad (45)$$

Because of $\partial_\rho \bar{p}_0 = \rho \partial_\rho \partial_\rho \bar{\psi}$, it follows that

$$\beta(\rho_g) = \frac{1}{2\rho_g(\rho_l - \rho_g)^2} \frac{\partial \bar{p}_0}{\partial \rho}(\rho_g), \quad (46a)$$

$$\beta(\rho_l) = \frac{1}{2\rho_l(\rho_l - \rho_g)^2} \frac{\partial \bar{p}_0}{\partial \rho}(\rho_l), \quad (46b)$$

which implies that $\beta(\rho_g)$ and $\beta(\rho_l)$ are directly related to the square of the sound speed $c_s^2 = \partial_\rho \bar{p}_0$ in the bulk phases, namely, the slopes at ρ_l and ρ_g in the \bar{p}_0 - ρ diagram. The mechanically stability condition requires that both the slopes should be positive, implying that $\beta(\rho_l) > 0$ and $\beta(\rho_g) > 0$. Generally speaking, $\beta(\rho_g)$ and $\beta(\rho_l)$ are not equal, and are computed from the given EOS.

We will prove that $\beta(\rho)$ generally could not be approximated by a linear function. To this end, we need to compute the first-order derivatives $\partial_\rho \beta$ at the bulk phases. The best way to evaluate $\partial_\rho \beta(\rho_l)$ is to employ the limit definition of the derivative:

$$\frac{\partial \beta}{\partial \rho}(\rho_l) = \lim_{\rho \rightarrow \rho_l} \frac{1}{\rho - \rho_l} \left[\frac{\bar{\psi}(\rho)}{(\rho - \rho_l)^2(\rho - \rho_g)^2} - \beta(\rho_l) \right]. \quad (47)$$

By noting that $\bar{\psi}(\rho_l) = 0$ and $\bar{\mu}_0(\rho_l) = \partial_\rho \bar{\psi}(\rho_l) = 0$, we obtain

$$\begin{aligned} \frac{\partial \beta}{\partial \rho}(\rho_l) &= \frac{1}{(\rho_l - \rho_g)^2} \lim_{\rho \rightarrow \rho_l} \frac{\bar{\psi}(\rho) - \beta(\rho_l)(\rho - \rho_l)^2(\rho - \rho_g)^2}{(\rho - \rho_l)^3} \\ &= \frac{1}{(\rho_l - \rho_g)^2} \lim_{\rho \rightarrow \rho_l} \frac{\bar{\mu}_0(\rho) - \beta(\rho_l)2(\rho - \rho_l)(\rho - \rho_g)(2\rho - \rho_l - \rho_g)}{3(\rho - \rho_l)^2} \\ &= \frac{1}{(\rho_l - \rho_g)^2} \lim_{\rho \rightarrow \rho_l} \frac{\frac{\partial^2 \bar{\psi}}{\partial \rho^2}(\rho) - \beta(\rho_l)[2(\rho - \rho_l)^2 + 2(\rho - \rho_g)^2 + 8(\rho - \rho_l)(\rho - \rho_g)]}{6(\rho - \rho_l)}. \end{aligned} \quad (48)$$

Then, due to Eqs. (46a) and (46b), the l'Hôpital rule can be applied once again to Eq. (48), which yields

$$\begin{aligned}\frac{\partial\beta}{\partial\rho}(\rho_l) &= \frac{1}{(\rho_l - \rho_g)^2} \lim_{\rho \rightarrow \rho_l} \frac{\frac{\partial^3\bar{\psi}}{\partial\rho^3}(\rho) - \beta(\rho_l)12(2\rho - \rho_l - \rho_g)}{6} \\ &= \frac{1}{6(\rho_l - \rho_g)^2} \left[\frac{\partial^3\bar{\psi}}{\partial\rho^3}(\rho_l) - 12\beta(\rho_l)(\rho_l - \rho_g) \right] \\ &= \frac{1}{6(\rho_l - \rho_g)^2} \left[\frac{\partial^3\bar{\psi}}{\partial\rho^3}(\rho_l) - \frac{6}{\rho_l - \rho_g} \frac{\partial^2\bar{\psi}}{\partial\rho^2}(\rho_l) \right],\end{aligned}\quad (49)$$

Similarly, the derivative $\partial_\rho\beta(\rho_g)$ can be evaluated as

$$\frac{\partial\beta}{\partial\rho}(\rho_g) = \frac{1}{6(\rho_l - \rho_g)^2} \left[\frac{\partial^3\bar{\psi}}{\partial\rho^3}(\rho_g) + \frac{6}{\rho_l - \rho_g} \frac{\partial^2\bar{\psi}}{\partial\rho^2}(\rho_g) \right].\quad (50)$$

Since the third-order derivative of $\bar{\psi}$ can be expressed as

$$\frac{\partial^3\bar{\psi}}{\partial\rho^3} = \frac{1}{\rho} \frac{\partial^2\bar{p}_0}{\partial\rho^2} - \frac{1}{\rho^2} \frac{\partial\bar{p}_0}{\partial\rho},\quad (51)$$

we obtain

$$\frac{\partial\beta}{\partial\rho}(\rho_l) = \frac{1}{6(\rho_l - \rho_g)^2} \left[\frac{1}{\rho_l} \frac{\partial^2\bar{p}_0}{\partial\rho^2}(\rho_l) - \frac{7\rho_l - \rho_g}{\rho_l^2(\rho_l - \rho_g)} \frac{\partial\bar{p}_0}{\partial\rho}(\rho_l) \right],\quad (52a)$$

$$\frac{\partial\beta}{\partial\rho}(\rho_g) = \frac{1}{6(\rho_l - \rho_g)^2} \left[\frac{1}{\rho_g} \frac{\partial^2\bar{p}_0}{\partial\rho^2}(\rho_g) + \frac{7\rho_g - \rho_l}{\rho_g^2(\rho_l - \rho_g)} \frac{\partial\bar{p}_0}{\partial\rho}(\rho_g) \right].\quad (52b)$$

It is proved that $\partial_\rho\beta(\rho_l)$ and $\partial_\rho\beta(\rho_g)$ are directly associated with both the slopes and curvatures at ρ_l and ρ_g in the \bar{p}_0 - ρ diagram.

Therefore, in addition to $\beta(\rho_l) \neq \beta(\rho_g)$, we could have different slopes at the two saturated phases, i.e., $\partial_\rho\beta(\rho_l) \neq \partial_\rho\beta(\rho_g)$, which implies that $\beta(\rho)$ could not be approximated or replaced by a simple linear function. We will show that the nonlinearity of $\beta(\rho)$ increases with the density ratio of two bulk phases. For low-density-ratio liquid-vapor flow, Eqs. (39), (46a), and (46b) provide three available choices [β_{CH} , $\beta(\rho_l)$, and $\beta(\rho_g)$] for the constant coefficient β_0 in the double-well approximation. We will make a direct comparison between the interfacial structures produced by the vdW EOS and the double-well approximation for the flat interface problem. The key point addressed in our paper is different from that of Jamet *et al.* [7] In their paper, the interfacial thickness is artificially enlarged while the surface tension and the speed of sound at the bulk phases are retained. They realize this goal at the price of using a modified EOS so that the original interfacial structure is not maintained. In contrast, our attention is paid to the alteration of the original interfacial structure due to the use of the double-well approximation.

VI. COMPARISON FOR A FLAT INTERFACE AT EQUILIBRIUM

A. Density ratio $\rho_l/\rho_g = 7.784$

First, we consider the same case as discussed in Sec. IV D with relatively high density ratio $\rho_l/\rho_g = 7.784$. According to the analysis in Sect. V, $\beta(\rho)$ serves as a nonlinear function of the fluid density. By applying Eqs. (46) and (52) to the vdW EOS in Eq. (34), we obtain $\beta(\rho_l) = 2.352 \times 10^{-3} > 0$ and $\beta(\rho_g) = 3.859 \times 10^{-3} > 0$, as well as the partial derivatives $\partial_\rho\beta(\rho_l) = 1.749 \times 10^{-4} > 0$ and $\partial_\rho\beta(\rho_g) = -1.599 \times 10^{-3} < 0$, which indeed show $\beta(\rho_l) \neq \beta(\rho_g)$ and $\partial_\rho\beta(\rho_l) \neq \partial_\rho\beta(\rho_g)$. In addition, the coefficient β_{CH} in Eq. (39) (derived by Cahn and Hilliard [34] in a sufficiently small vicinity of the critical point) is equal to 1.874×10^{-3} .

In Fig. 2(a), we plot the coefficient $\beta(\rho)$ as a function of ρ in the range $(0, b^{-1})$, which is divided into three parts by the two saturated points A, $(\rho_g, \beta(\rho_g))$, and B, $(\rho_l, \beta(\rho_l))$. The tangent lines are marked at these two points according to the slopes $\partial_\rho\beta(\rho_l)$ and $\partial_\rho\beta(\rho_g)$, which are consistent with the variation of $\beta(\rho)$. The nonlinear variation of $\beta(\rho)$ between the saturated points A and B is directly related to the static structure of the transition region, which will be influenced by the approximation with constant coefficient. Figure 2(b) shows the bulk free energy density $\bar{\psi}(\rho)$ obtained from the double-well approximations [with three different coefficients $\beta(\rho_l)$, $\beta(\rho_g)$, and β_{CH} for β_0] and the analytical solution obtained from the vdW EOS. The comparison indicates that the double-well approximation is sensitive to the choice of the constant coefficient β_0 , particularly in the transition region between the two bulk phases. We observe that the results with both $\beta_0 = \beta(\rho_l)$ and $\beta_0 = \beta_{CH}$ are close to the analytical solutions obtained from the vdW EOS, while the latter (with $\beta_0 = \beta_{CH}$) shows larger discrepancies. Moreover, the result with $\beta_0 = \beta(\rho_g)$ shows more obvious difference compared to that with $\beta_0 = \beta_{CH}$. Since $\bar{p}_0(\rho)$ is directly determined by $\bar{\psi}(\rho)$, similar features can be observed in Fig. 2(c).

Figure 3 demonstrates the spatial distributions of different physical quantities in the transition region. It is found that all the physical quantities are well approximated by the double-well approximation with the constant coefficient $\beta_0 = \beta(\rho_l)$, showing small visible deviations from the analytical solutions. As illustrated in Fig. 3(a), the slope of density profile increases by the use of $\beta_0 = \beta(\rho_g)$ and decreases if $\beta_0 = \beta_{CH}$ is applied. For other three quantities including the bulk free energy density $\bar{\psi}$, the thermodynamic pressure \bar{p}_0 and the capillary stress $-\kappa\rho(d^2\rho/dx^2)$, the resulting profiles with $\beta_0 = \beta(\rho_g)$ are not in good agreement with the analytical solutions, with overestimated magnitudes near the peak and valley points, as displayed in Figs. 3(b)–3(d). Nevertheless, the overall trends of the variations are correctly given by $\beta_0 = \beta(\rho_g)$. Compared to $\beta_0 = \beta(\rho_g)$, the results obtained from $\beta_0 = \beta_{CH}$ are closer to the analytical solutions. The comparison indicates that, for relatively high density ratio ($\rho_l/\rho_g = 7.784$), the predictions with the double-well approximation are very sensitive to choice of the constant β_0 due to relatively strong nonlinear variation of $\beta(\rho)$ in the transition region.

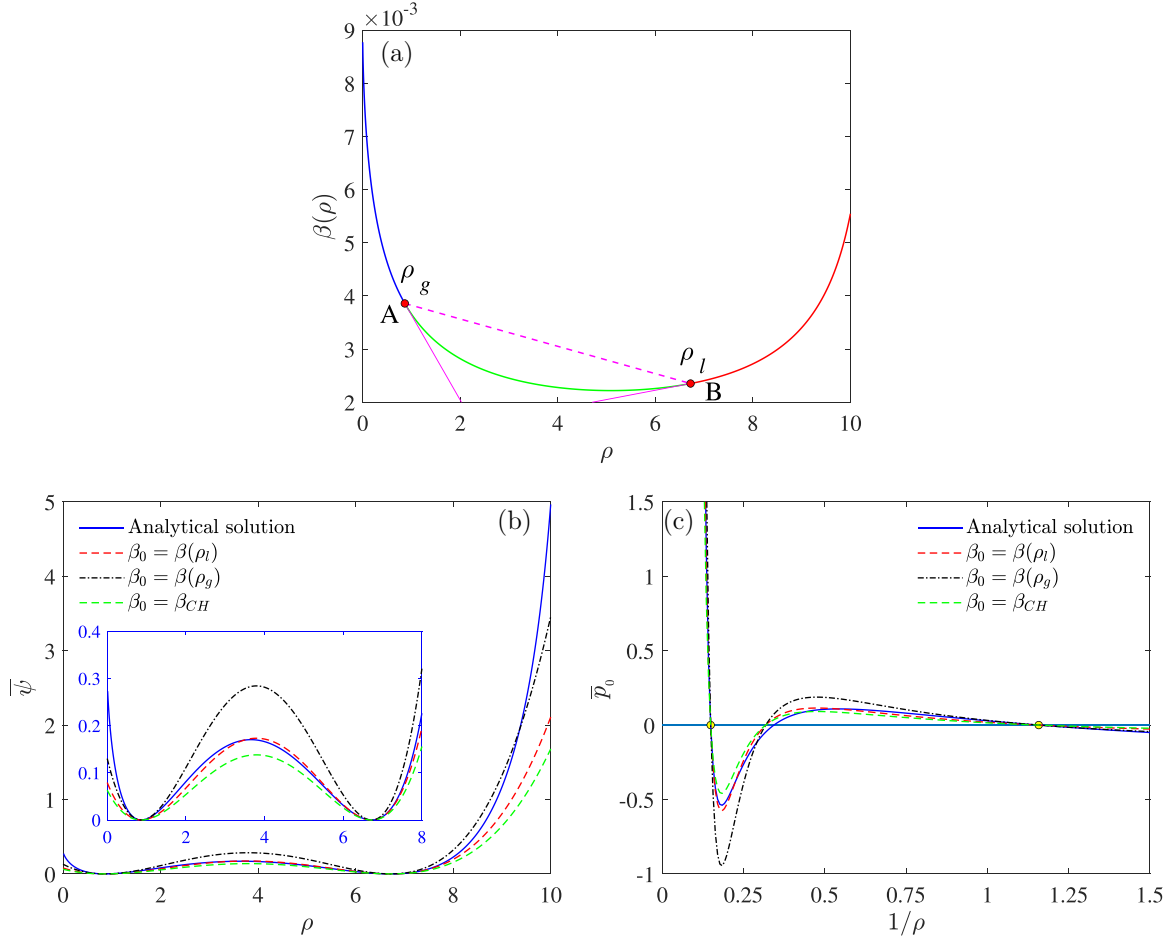


FIG. 2. Comparison of the analytical solution and the double-well approximation with constant coefficients [$\beta(\rho_l)$, $\beta(\rho_g)$ and β_{CH}]. The analytical solution as well as the coefficients $\beta(\rho_g)$ and $\beta(\rho_l)$ are obtained from the vdW EOS. (a) Coefficient function $\beta(\rho)$ at fixed temperature T . A: $(\rho_g, \beta(\rho_g))$; B: $(\rho_l, \beta(\rho_l))$. (b) Redefined bulk free energy density $\bar{\psi}(\rho)$. (c) Thermodynamic pressure \bar{p}_0 as a function of ρ^{-1} .

B. Density ratio $\rho_l/\rho_g = 1.774$

Second, by increasing the temperature to $T = 0.56$, the liquid and vapor densities are evaluated as $\rho_l = 4.513$ and $\rho_g = 2.543$, whose ratio is $\rho_l/\rho_g = 1.774$. By using Eqs. (46) and (52), we obtain $\beta(\rho_l) = 1.845 \times 10^{-3} > 0$ and $\beta(\rho_g) = 2.074 \times 10^{-3} > 0$, as well as the partial derivatives $\partial_\rho \beta(\rho_l) = -2.967 \times 10^{-5} < 0$ and $\partial_\rho \beta(\rho_g) = -2.300 \times 10^{-4} < 0$, which also show $\beta(\rho_l) \neq \beta(\rho_g)$ and $\partial_\rho \beta(\rho_l) \neq \partial_\rho \beta(\rho_g)$. The bulk thermodynamic pressure and chemical potential are $p^* = 0.691$ and $\mu^* = -0.834$, respectively. The coefficient β_{CH} (evaluated at the critical point) is still equal to 1.874×10^{-3} .

Figure 4(a) shows the variation of $\beta(\rho)$ with respect to the density ρ . Compared to the first case, the density ratio is smaller so that the nonlinearity feature of $\beta(\rho)$ between A, $(\rho_g, \beta(\rho_g))$, and B, $(\rho_l, \beta(\rho_l))$, is greatly weakened. With different coefficients $\beta_0 = \beta(\rho_l)$, $\beta_0 = \beta(\rho_g)$ and β_{CH} , the bulk free energy density potential $\bar{\psi}(\rho)$ and the thermodynamic pressure $\bar{p}_0(\rho)$ are displayed in Figs. 4(b) and 4(c). It is observed that the results obtained from the double-well approximations with different coefficients are in good agreement with the analytical solution from vdW EOS between ρ_l and ρ_g . Furthermore, we also compare the static structures of

different physical quantities in the transition region, as displayed in Fig. 5. Compared to the case with relatively high density ratio $\rho_l/\rho_g = 7.784$, all the density profiles agree very well with each other, as shown in Fig. 5(a). For $\bar{\psi}$, \bar{p}_0 , and $-\kappa \rho(d^2 \rho/dx^2)$, the double-well approximations with $\beta_0 = \beta(\rho_l)$ and $\beta_0 = \beta(\rho_g)$ mainly yield small discrepancies near the peak and valley points, especially for those with $\beta_0 = \beta(\rho_g)$. The results with $\beta_0 = \beta_{CH}$ appear closer to the analytical solution than other results. This is reasonable because β_{CH} is originally derived in a small vicinity of the critical point.

The comparison shows that for near-critical fluids (relatively low density ratio $\rho_l/\rho_g = 1.774$), the double-well approximation with constant coefficients ($\beta_0 = \beta(\rho_l)$, $\beta(\rho_g)$ and β_{CH}) can achieve satisfactory predictions to static structures in the transition region when compared to the analytical solution obtained from the vdW EOS.

However, the above analysis and conclusions are restricted to a stationary flat interface, where the effects of surface curvature and complex interfacial dynamics are not involved. In addition, the particularity of 1D problem takes effect in the simplification (for example, the surface tension stress tensor $\Phi = \mathbf{0}$ holds for the 1D problem). With the double-well

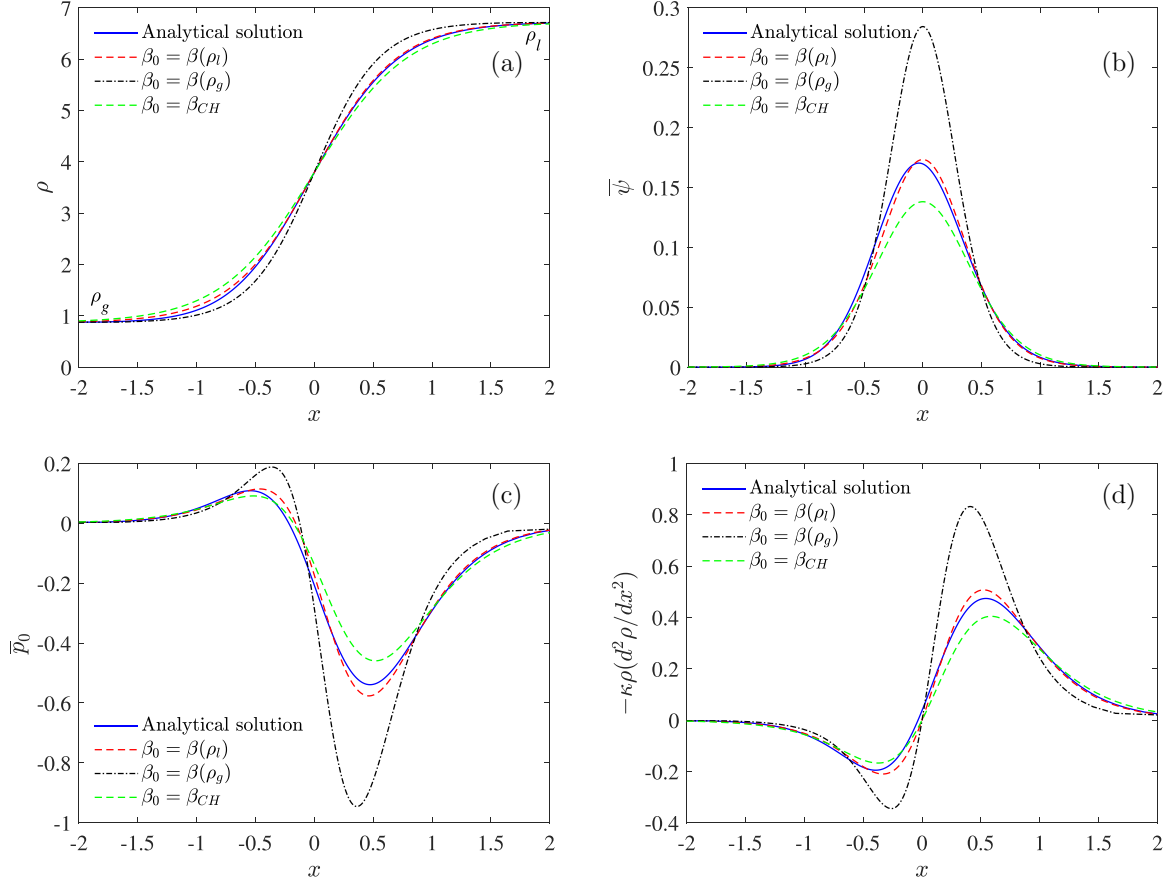


FIG. 3. Comparison between the analytical solution and the double-well approximations with constant coefficients $[\beta(\rho_l), \beta(\rho_g)$ and $\beta_{CH}]$. (a) Density ρ ; (b) bulk free energy density ψ ; (c) thermodynamic pressure \bar{p}_0 ; (d) capillary stress $-\kappa\rho(d^2\rho/dx^2)$.

approximation in Eq. (38), it is known that Eq. (16) admits an asymptotic solution, which exhibits a hyperbolic tangent distribution [Eq. (40)] at equilibrium. In the limit of low-density ratio, this asymptotic solution yields a good approximation to the density distribution corresponding to the given EOS. For complex two-phase hydrodynamics, theoretical analysis is usually difficult to carry out. The bulk densities could also be influenced by the fluid-solid interaction and the surface wettability. Whether the theoretical relations derived for a flat interface at equilibrium could be approximately applied to simulate complex interfacial flows remains a question. To our knowledge, direct comparison of the numerical results obtained from the given EOS and its double-well approximation has not been reported previously.

VII. COMPARISON FOR COMPLEX TWO-PHASE FLOWS

To demonstrate the applicability of the double-well approximation for near-critical fluids (low-density-ratio limit), we will simulate a droplet impact on a hydrophilic wall with the prescribed contact angle $\theta_w = \pi/3$ based on the following considerations. On one hand, in addition to the unsteady effect, the physical complexity of this problem is attributed to fluid-solid interaction and interfacial vorticity dynamics associated with the moving and deforming interface. On the other hand, direct numerical comparison between the double-well approximation and the given EOS is not found in the existing

literature, although both of them have been widely applied in different numerical tests. In order to realize a convincing comparison, both the choice of the computational method and the design of simulation cases are significant.

A. A brief introduction of WB-DUGKS

Recently, Guo [10] proposed the well-balanced lattice Boltzmann model (WB-LBM), which was later extended by Zeng *et al.* [23] to the well-balanced discrete unified gas kinetic scheme (WB-DUGKS). Compared to the existing methods, their numerical tests showed that the spurious velocity for a stationary droplet can be completely eliminated with the WB-DUGKS, whose superior ability to capture a moving surface was also validated. This motivates us to apply this approach to the present simulation. Since the technical details of the WB-DUGKS are described in their paper, only a brief introduction to the WB-DUGKS is provided below.

In the WB-DUGKS, the following discrete Boltzmann model is solved:

$$\frac{\partial f_\alpha}{\partial t} + \xi_\alpha \cdot \nabla f_\alpha = \frac{f_\alpha^{eq} - f_\alpha}{\tau} + F_\alpha, \quad \alpha = 0, \dots, Q-1, \quad (53)$$

where $f_\alpha \equiv f(\mathbf{x}, \xi_\alpha, t)$ is the particle distribution function with the discrete particle velocity ξ_α at the spatial location \mathbf{x} and time t . The subscript α denotes the discrete particle

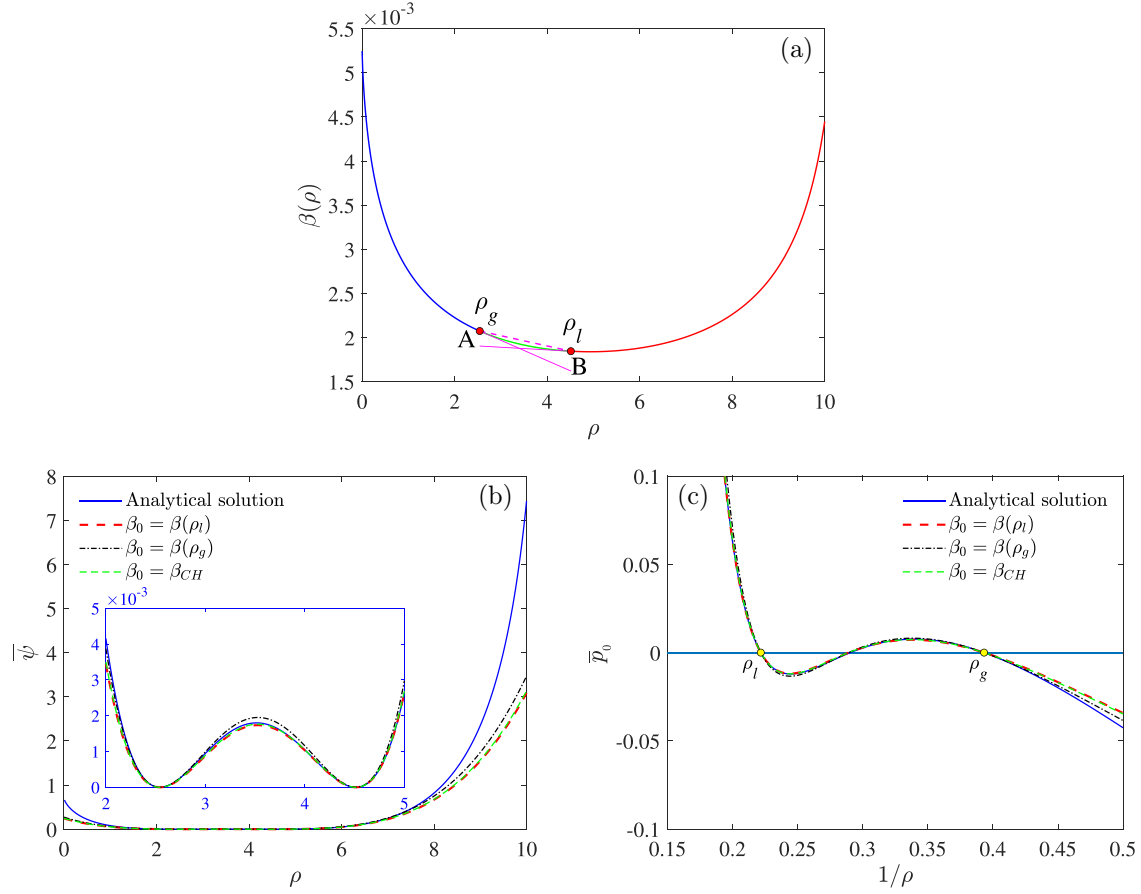


FIG. 4. Comparison of the analytical solution and the double-well approximation with constant coefficients [$\beta(\rho_l)$, $\beta(\rho_g)$, and β_{CH}]. The analytical solution as well as the coefficients $\beta(\rho_g)$ and $\beta(\rho_l)$ are obtained from the vdW EOS. (a) Coefficient function $\beta(\rho)$ at fixed temperature T . A: $(\rho_g, \beta(\rho_g))$; B: $(\rho_l, \beta(\rho_l))$. (b) Redefined bulk free energy density $\bar{\psi}(\rho)$. (c) Thermodynamic pressure \bar{p}_0 as a function of ρ^{-1} .

velocity direction and Q is the total number of discrete particle velocities used. τ is the relaxation time, which is related to the kinematic viscosity ν through the relation $\nu = c_s^2 \tau$. $c_s = \sqrt{RT}$ is the speed of sound, R is the gas constant, and T is the temperature.

The equilibrium distribution function f_α^{eq} is designed as

$$f_\alpha^{eq} = \begin{cases} \rho - (1 - \omega_0)\rho_0 + \omega_0 \rho s_0(\mathbf{u}), & \alpha = 0, \\ \omega_\alpha [\rho_0 + \rho s_\alpha(\mathbf{u})], & \alpha \neq 0, \end{cases} \quad (54)$$

where ρ_0 is a numerical constant, ω_α ($\alpha = 0, \dots, Q-1$) are the weighting factors, and $s_\alpha(\mathbf{u})$ is given by

$$s_\alpha(\mathbf{u}) = \frac{\boldsymbol{\xi}_\alpha \cdot \mathbf{u}}{c_s^2} + \frac{(\boldsymbol{\xi}_\alpha \cdot \mathbf{u})^2}{2c_s^4} - \frac{\mathbf{u} \cdot \mathbf{u}}{2c_s^2}. \quad (55)$$

The choice of ρ_0 may influence the stability of the numerical scheme by ensuring the positivity of the equilibrium, but does not influence the results. Following Zeng *et al.* [23], we set $\rho_0 = 0$ in the simulations. The well-known D2Q9 discrete particle velocity model is adopted ($c_s^2 = RT$, $\omega_0 = 4/9$, $\omega_{1,2,3,4} = 1/9$, and $\omega_{5,6,7,8} = 1/36$). Compared to the Maxwellian distribution function, the second-order moment of this new equilibrium distribution $\sum_{\alpha=0}^{Q-1} \boldsymbol{\xi}_\alpha \boldsymbol{\xi}_\alpha f_\alpha^{eq}$ is equal to $\rho \mathbf{u} \mathbf{u}$ instead of $c_s^2 \rho \mathbf{I} + \rho \mathbf{u} \mathbf{u}$. Therefore, differently from the standard lattice Boltzmann equation (LBE), $-\nabla \cdot (c_s^2 \rho)$ does

not appear in the recovered hydrodynamic equations for the present model. In addition, the mesoscopic forcing term F_α is designed as

$$F_\alpha = \omega_\alpha \left[\frac{\boldsymbol{\xi}_\alpha \cdot (-\rho \nabla \mu_\rho)}{c_s^2} + \frac{\mathbf{u} \cdot (-\rho \nabla \mu_\rho + c_s^2 \nabla \rho) : (\boldsymbol{\xi}_\alpha \boldsymbol{\xi}_\alpha - c_s^2 \mathbf{I})}{c_s^4} + \frac{1}{2} \left(\frac{\boldsymbol{\xi}_\alpha^2}{c_s^2} - D \right) (\mathbf{u} \cdot \nabla \rho) \right], \quad (56)$$

where D is the spatial dimension and $D = 2$ for the D2Q9 model.

Through the Chapman-Enskog analysis, Eqs. (5a) and (5b) can be recovered from the present model at the continuum limit, but the resulting viscous stress tensor $\boldsymbol{\Pi}$ has a fixed bulk-to-shear viscosity ratio $\mu_\nu/\mu = (D+2)/D$ [which corresponds to a term $\rho \tau c_s^2 (\nabla \cdot \mathbf{u}) \mathbf{I}$]. However, combining the Chapman-Enskog expansion and the Hermite expansion [37], we find that this restriction on the ratio of bulk to shear viscosity can be removed by adding another source term $\omega_\alpha \frac{1}{2} \left(\frac{D+2}{D} - \frac{\mu_\nu}{\mu} \right) \rho \nabla \cdot \mathbf{u} \left(\frac{\boldsymbol{\xi}_\alpha^2}{c_s^2} - D \right)$ to the mesoscopic forcing term F_α .

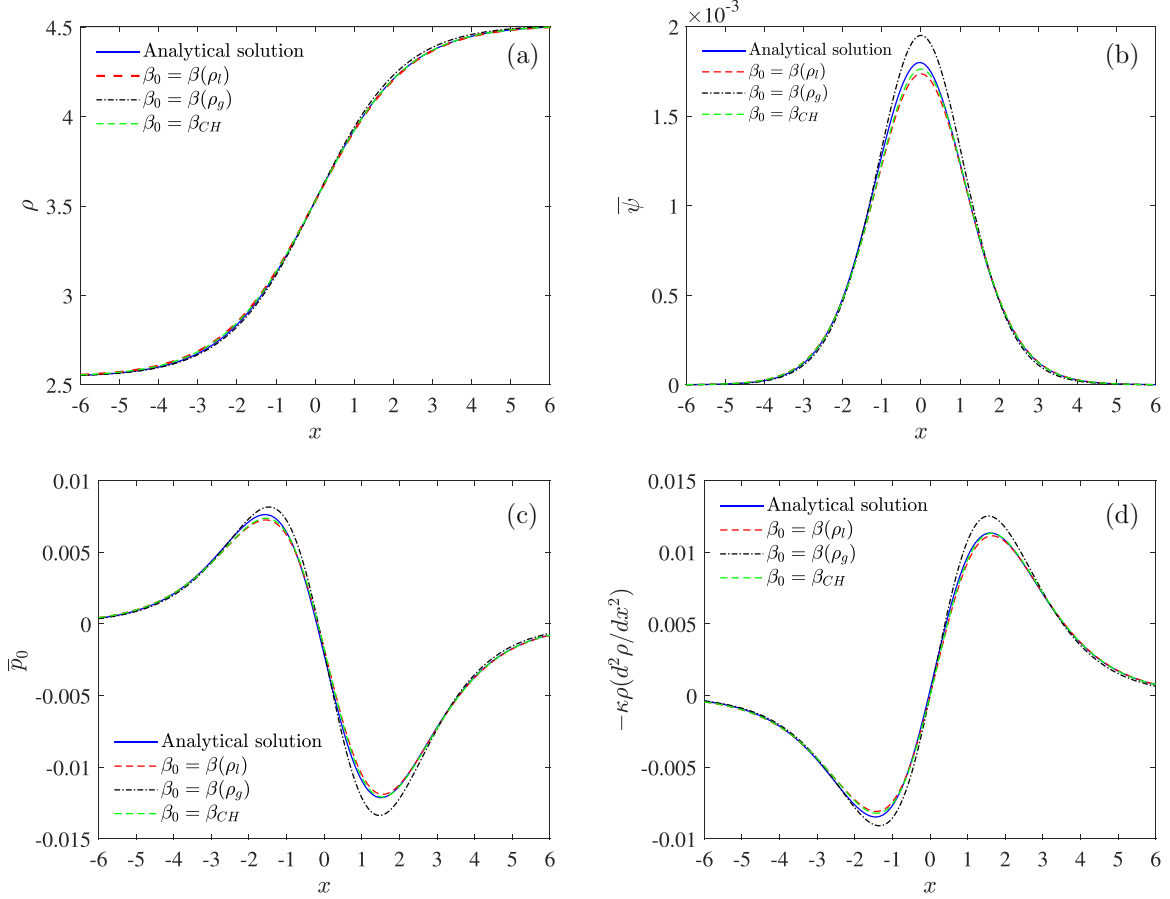


FIG. 5. Comparison between the analytical solution and the double-well approximations with constant coefficients [$\beta(\rho_l)$, $\beta(\rho_g)$, and β_{CH}]. (a) Density ρ ; (b) bulk free energy density ψ ; (c) thermodynamic pressure \bar{p}_0 ; (d) capillary stress $-\kappa\rho(d^2\rho/dx^2)$.

B. Problem description

As illustrated in Fig. 6(a), a liquid droplet with the diameter D_l centered at the location $(x_0, y_0) = (D_l/2, 2D_l)$ is surrounded by the vapor, where (x, y) represent the vertical and horizontal coordinates and the z axis is perpendicular to the plane of the diagram. The droplet radius is denoted as $R_l = D_l/2$.

The density field is initialized by

$$\rho(x, y) = \rho_l\phi(x, y) + \rho_g[1 - \phi(x, y)], \quad (57)$$

with the shape function $\phi(x, y)$ given as

$$\begin{aligned} \phi(x, y) &= \frac{1}{2} \left[1 + \tanh \left(\frac{2(R_l - \sqrt{(x - x_0)^2 + (y - y_0)^2})}{W} \right) \right], \end{aligned} \quad (58)$$

where the saturated densities ρ_l and ρ_g are determined according to the Maxwell equal-area rule [see Eq. (28)]. The interfacial thickness parameter W is determined by the first equation in (41) with known κ and β_0 . The second equation in (41) gives an estimated surface tension coefficient σ_s . For the

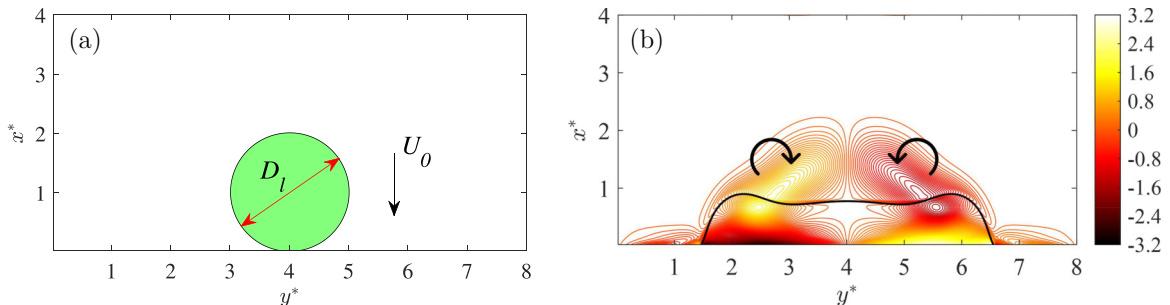


FIG. 6. (a) Sketch of the initial state of the droplet contacting with the wall. D_l is the droplet diameter and U_0 represents the magnitude of the initial impact velocity. (b) Droplet interface with background vorticity field at $t^* = 0.8$. $We = 85.7$, and $Re = 100$.

low-Mach number case, except for the density and viscosity ratios, the two-phase flow system is mainly controlled by the Weber number We and the Reynolds number Re :

$$We = \frac{\rho_l U_0^2 D_l}{\sigma_s}, \quad Re = \frac{\rho_l U_0 D_l}{\mu_l}. \quad (59)$$

Therefore, for fixed Weber and Reynolds numbers, the initial velocity field $\mathbf{u} = (u_x, u_y)$ is $u_x(x, y) = -U_0 \phi(x, y)$ and $u_y(x, y) = 0$, where $U_0 = (We \sigma_s / (\rho_l D_l))^{1/2}$ is a constant velocity in the bulk region of the liquid phase. Then, the relaxation time is evaluated through $\tau = U_0 D_l / (Re c_s^2)$.

Periodic boundary conditions are considered in the horizontal y direction. In the vertical x direction, the on-wall bounce back scheme is applied to the bottom wall while the outflow boundary condition is used for the top boundary. The geometrical wetting boundary condition (proposed by Ding *et al.* [38], further applied by Liang *et al.* [17] and Yang *et al.* [39]) is used to describe the wettability of the ideal solid wall with a given contact angle θ_w , namely,

$$\mathbf{n}_w \cdot \nabla \rho = -\tan\left(\frac{\pi}{2} - \theta_w\right) \|\nabla \rho - (\mathbf{n}_w \cdot \nabla \rho) \mathbf{n}_w\|, \quad (60)$$

where \mathbf{n}_w is the unit normal vector pointing from the wall to the fluid. Equation (60) is essentially a Neumann boundary condition, which relates the wall-normal density gradient to its tangential gradient at the wall. With the implementation of Eq. (60), the second-order isotropic central schemes [17,26] are used to compute $\nabla \rho$ and $\nabla^2 \rho$ at all the cell centers. In this paper, a hydrophilic ideal wall with $\theta_w = \pi/3$ is considered.

C. Simulations and discussions

Six simulations (Cases A–F) are carried out by using the WB-DUGKS with the Weber number $We = 85.7$ and the Reynolds number $Re = 100$. For all the simulated cases, the density ratio is as $\rho_l/\rho_g = 1.174$ with $\rho_l = 4.513$ and $\rho_g = 2.543$ at $T = 0.56$, which is the same as that used for a flat interface at equilibrium. The interfacial free energy coefficient is $\kappa = 0.02$ for all the cases. Since the dynamic viscosity is $\mu = \rho \nu = \rho c_s^2 \tau$, a constant relaxation time τ implies that the ratio of the dynamic viscosity is $\mu_l/\mu_g = 1.174$ and that the kinematic viscosity ratio is $\nu_l/\nu_g = 1$. The domain size is $L_x \times L_y = 200\Delta x \times 400\Delta x$, where $\Delta x = 1$ is the grid spacing. The droplet diameter D_l is equal to $100\Delta x$.

For Case A, the double-well approximation with $\beta_0 = \beta(\rho_l) = 1.845 \times 10^{-3}$ is used, which gives the interfacial thickness W and the surface tension coefficient σ_s as $W = 4.728$ and $\sigma_s = 0.01094$, respectively. It is noted that the empirical condition ($W > 3\Delta x = 3$) for numerically sustainable interfacial thickness is satisfied. Then, the initial velocity is computed as $U_0 = 0.0492$, which implies a small Mach number $Ma = U_0/\sqrt{RT} = 0.0658$ that is compatible with the isothermal assumption. Therefore, the resulting Knudsen number is $Kn \equiv Ma/Re = 7.676 \times 10^{-4}$ so that the flow entirely lies in the continuum regime. The ratio of the time step Δt to the relaxation time τ is $\Delta t/\tau = 0.975$ ($\Delta t = 0.1$ and $\tau = 0.1026$). The parameters for Case B are the same as those used in Case A except that the vdW EOS with $a = 9/49$, $b = 2/21$, and $R = 1$ is applied.

Similarly, for Case C, we adopt the double-well approximation with $\beta_0 = \beta(\rho_g) = 2.074 \times 10^{-3}$, which yields slightly different parameters $W = 4.459$ and $\sigma_s = 0.01160$. In order to retain consistent Weber and Reynolds numbers (as used in Cases A and B), U_0 and τ should be adjusted to 0.0507 and 0.1056, respectively. As a result, the Mach and Knudsen numbers become $Ma = 0.0677$ and $Kn = Ma/Re = 7.904 \times 10^{-4}$ (continuum regime). The ratio of the time step Δt to the relaxation time τ is $\Delta t/\tau = 0.947$. Case D adopts the same parameters as Case C with the vdW EOS. The double-well approximation with $\beta_0 = \beta_{CH} = 1.874 \times 10^{-3}$ is used for Case E, while the vdW EOS is applied for Case F with other parameters kept the same as Case E.

Figure 6(b) displays the location of the droplet interface at $t^* = 0.8$ superposed on the normalized vorticity ω_z^* as the background field. High-vorticity-magnitude regions are observed near the bottom wall due to the strong shearing effects during the spreading process. In addition, two counter-rotating vortices are formed around the droplet interface due to the outside downward flow near the centerline and the stretching motion of the interface towards opposite directions. Figure 7 shows the evolution of the droplet morphology during droplet-wall interaction for the four simulated cases. Due to the large adhesive force between the droplet and the hydrophilic wall, their contact area increases with time. The results for different cases are in excellent agreement except for small visible differences near the centerline, which indicates that the double-well approximation provides a good approximation in predicting the time evolution of the droplet morphology.

We also compare the distributions of different macroscopic quantities at $t^* = 0.8$. Figure 8 shows the distributions of physical quantities at $x^* = 1$ (a horizontal line outside the droplet). As shown in Fig. 8(a), the normalized vertical velocity component u_x^* exhibits distinct peak and valley regions along this line. The high negative peak corresponds to the downward flow near the centerline while the other two positive peaks representing the upwelling flow, which are induced by the two counter-rotating vortices as marked in Fig. 6(b). These features are also consistent with the distributions of the normalized horizontal velocity component u_y^* shown in Fig. 8(b). For u_x^* and u_y^* , we find that the results of Cases A and E [double-well approximation with $\beta_0 = \beta(\rho_l)$ and β_{CH}] obviously deviate from those of Cases B–D and F especially near the peak and valley points. Despite these discrepancies in their magnitudes, all the results are qualitatively consistent.

Surprisingly, as illustrated in Fig. 8(c), the normalized vorticity component values ω_z^* are in excellent agreement among different cases, and are not evidently influenced by the double-well approximations of the EOS. As for the normalized density ρ^* shown in Fig. 8(d), Cases B and D with vdW EOS agree well with each other only with minor difference. In contrast, the density distributions provided by the double-well approximations (Cases A, C, and E) show obvious differences especially near the two peak vorticity regions, where the density and velocity fields are more strongly coupled compared to other common regions. However, the overall trend of the density variation is correctly predicted by the double-well approximations.

Moreover, Fig. 9 compares the distributions of physical quantities at the left limiting position of the centerline, i.e.,

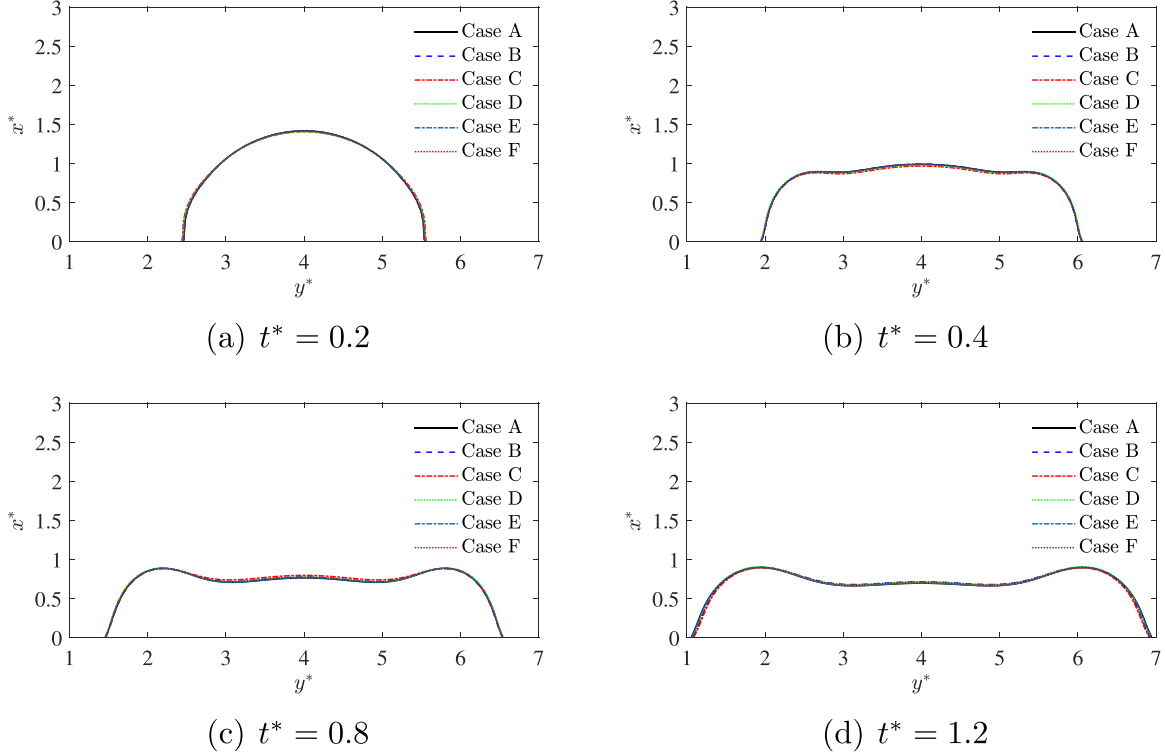


FIG. 7. Comparison of droplet morphologies at different dimensionless time instants. The interface is defined as the isosurface with the density $\rho_l \equiv (\rho_l + \rho_g)/2$. (a) $t^* = 0.2$, (b) $t^* = 0.4$, (c) $t^* = 0.8$, and (d) $t^* = 1.2$. $We = 85.7$ and $Re = 100$.

$y^* \rightarrow 4$ (a vertical line across the droplet). As shown in Fig. 9(a), compared to the results of Cases B, D, and F with vdW EOS, the double-well approximations (Cases A, C, and E) yield some deviations in different portions of the curves, while the overall trends of different cases are very similar and acceptable. Figures 9(b) and 9(c) display the comparisons for the normalized vertical velocity component u_y^* and the normalized vorticity component ω_z^* , where excellent agreements among different cases are achieved. As for the normalized density ρ^* in Fig. 9(d), the results of Cases A, B, and D–F agree well with each other while Case C [with $\beta_0 = \beta(\rho_g)$] shows relatively lower liquid density inside the droplet. The remaining portions of the density profiles remain consistent for all the simulated cases. The normalized saturated densities for a flat interface at equilibrium are also marked in Fig. 9(d) for reference. It is observed that the densities of the spreading droplet do not deviate much from these saturated ones in the low-Mach-number limit.

We summarize as follows. For near-critical fluids (low-density-ratio limit), we realize a direct comparison between the double-well approximation with constant coefficient β_0 [as determined by Eqs. (39) and (46a), (46b), originally derived from a flat surface at equilibrium] and the vdW EOS by using a recently proposed WB-DUGKS. On one hand, the comparison indicates that, for unsteady complex interfacial dynamics, the double-well approximation can yield satisfactory results for important macroscopic quantities with small discrepancies when compared to the given vdW EOS. On the other hand, even for unsteady interfacial motion, the comparison justifies the local equilibrium assumption of the density

distribution in the transition region, which can be well approximated with a hyperbolic tangent solution asymptotically.

VIII. MEAN FIELD FORCE AND ITS SIMPLIFICATIONS

The above sections concentrate on the discussion of the EOS and its double-well approximation. Another important aspect of two-phase flow modeling is the simplification of the mean field force, which includes both the pressure drop in the EOS and the surface tension force caused by the long-range molecular interaction.

Following the previous studies on kinetic theory of two-phase flow [40–43], we consider identical spherical particles with mass m that interact through the isotropic Sutherland’s potential

$$V(r) = \begin{cases} +\infty, & r < \sigma, \\ -\frac{\phi_\sigma}{m^2} \left(\frac{r}{\sigma}\right)^{-\gamma_p}, & r \geq \sigma, \end{cases} \quad (61)$$

where σ is the effective molecular diameter, m is the molecular mass, and $\mathbf{r} = \mathbf{x}_1 - \mathbf{x}$ is the relative position vector of two colliding particles at \mathbf{x} and \mathbf{x}_1 , respectively. $r = \|\mathbf{r}\|$ denotes the magnitude of \mathbf{r} . ϕ_σ/m^2 denotes the depth of potential well at $r = \sigma$. This potential can be viewed as the superposition of a hard-sphere repulsive potential for $r < \sigma$ and an attractive soft potential tail for $r \geq \sigma$. The parameter γ_p is the order of the power potential tail, which is used to control the range of attractive interaction. The hard-sphere repulsive potential is responsible for the phase separation while the attractive soft

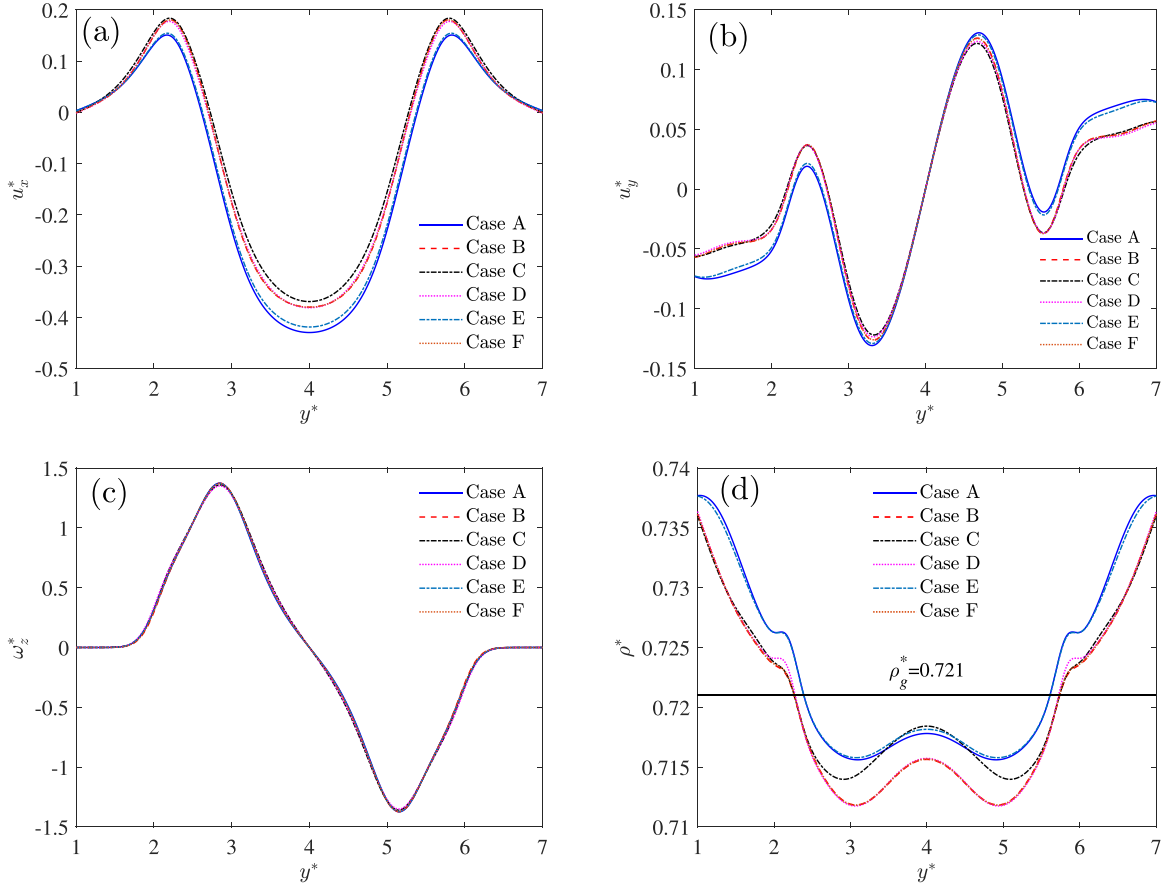


FIG. 8. Comparison of the normalized (a) vertical velocity component $u_x^* \equiv u_x/U$, (b) horizontal velocity component $u_y^* \equiv u_y/U$, (c) vorticity component $\omega_z^* \equiv \omega_z/(U/R)$, and (d) density $\rho^* = \rho/\rho_l$ at $x^* = 1$ along the horizontal direction. $\rho_l \equiv (\rho_l + \rho_g)/2$ is defined as the interfacial density. We = 85.7 and Re = 100.

potential tail influences both the EOS and the surface tension force.

For a fixed time t , we use \mathbf{F}_m to denote the mean-field force per unit mass acting on a molecule at the location \mathbf{x} by all the surrounding particles at the locations \mathbf{x}_1 out of the effective spherical domain [43], namely,

$$\mathbf{F}_m(\mathbf{x}, t) = \int_{\|\mathbf{x}_1 - \mathbf{x}\| > \sigma} \frac{dV}{dr}(r) \frac{\mathbf{x}_1 - \mathbf{x}}{\|\mathbf{x}_1 - \mathbf{x}\|} \rho(\mathbf{x}_1, t) d\mathbf{x}_1. \quad (62)$$

Equivalently, by using the relative position vector \mathbf{r} as the integration variable, Eq. (62) can be rewritten as

$$\mathbf{F}_m(\mathbf{x}, t) = \int_{r > \sigma} \frac{dV}{dr}(r) \frac{\mathbf{r}}{r} \rho(\mathbf{x} + \mathbf{r}, t) d\mathbf{r}. \quad (63)$$

Supposing that the density is a slowly varying variable, the smooth density approximation can be applied to $\rho(\mathbf{x} + \mathbf{r})$ (the variable t is omitted for simplicity) by performing the Taylor-series expansion at the location \mathbf{x} . Up to the third order, we have

$$\begin{aligned} \rho(\mathbf{x} + \mathbf{r}) &= \rho(\mathbf{x}) + r_k \frac{\partial \rho}{\partial x^k}(\mathbf{x}) + \frac{1}{2} r_j r_k \frac{\partial^2 \rho}{\partial x_j \partial x_k}(\mathbf{x}) \\ &+ \frac{1}{6} r_k r_s r_q \frac{\partial^3 \rho}{\partial x_k \partial x_s \partial x_q}(\mathbf{x}). \end{aligned} \quad (64)$$

Substituting Eq. (64) into Eq. (63) gives

$$\begin{aligned} (\mathbf{F}_m)_j &= \left[\int_{r > \sigma} \frac{dV}{dr} \frac{r_j r_k}{r} d\mathbf{r} \right] \frac{\partial \rho}{\partial x_k}(\mathbf{x}) \\ &+ \left[\frac{1}{6} \int_{r > \sigma} \frac{dV}{dr} \frac{r_j r_k r_s r_q}{r} d\mathbf{r} \right] \frac{\partial^3 \rho}{\partial x_k \partial x_s \partial x_q}(\mathbf{x}). \end{aligned} \quad (65)$$

If $\gamma_p > 3$, the first coefficient on the right-hand side of Eq. (65) converges, i.e.,

$$\int_{r > \sigma} \frac{dV}{dr} \frac{r_j r_k}{r} d\mathbf{r} = \frac{4\pi\sigma^3 \phi_\sigma}{3} \frac{\gamma_p}{m^2 \gamma_p - 3} \delta_{jk}. \quad (66)$$

If $\gamma_p > 5$, the second coefficient on the right-hand side of Eq. (65) converges, which results in

$$\begin{aligned} \frac{1}{6} \int_{r > \sigma} \frac{dV}{dr} \frac{r_j r_k r_s r_q}{r} d\mathbf{r} \\ = \frac{2}{45} \pi \sigma^5 \frac{\phi_\sigma}{m^2 \gamma_p - 5} (\delta_{js} \delta_{kq} + \delta_{jk} \delta_{sq} + \delta_{jq} \delta_{sk}). \end{aligned} \quad (67)$$

Therefore, when the controlling parameter satisfies the requirement $\gamma_p > 5$, \mathbf{F}_m can be expressed as

$$\mathbf{F}_m = -\nabla V_m, \quad V_m = -2a\rho - \kappa \nabla^2 \rho, \quad (68)$$

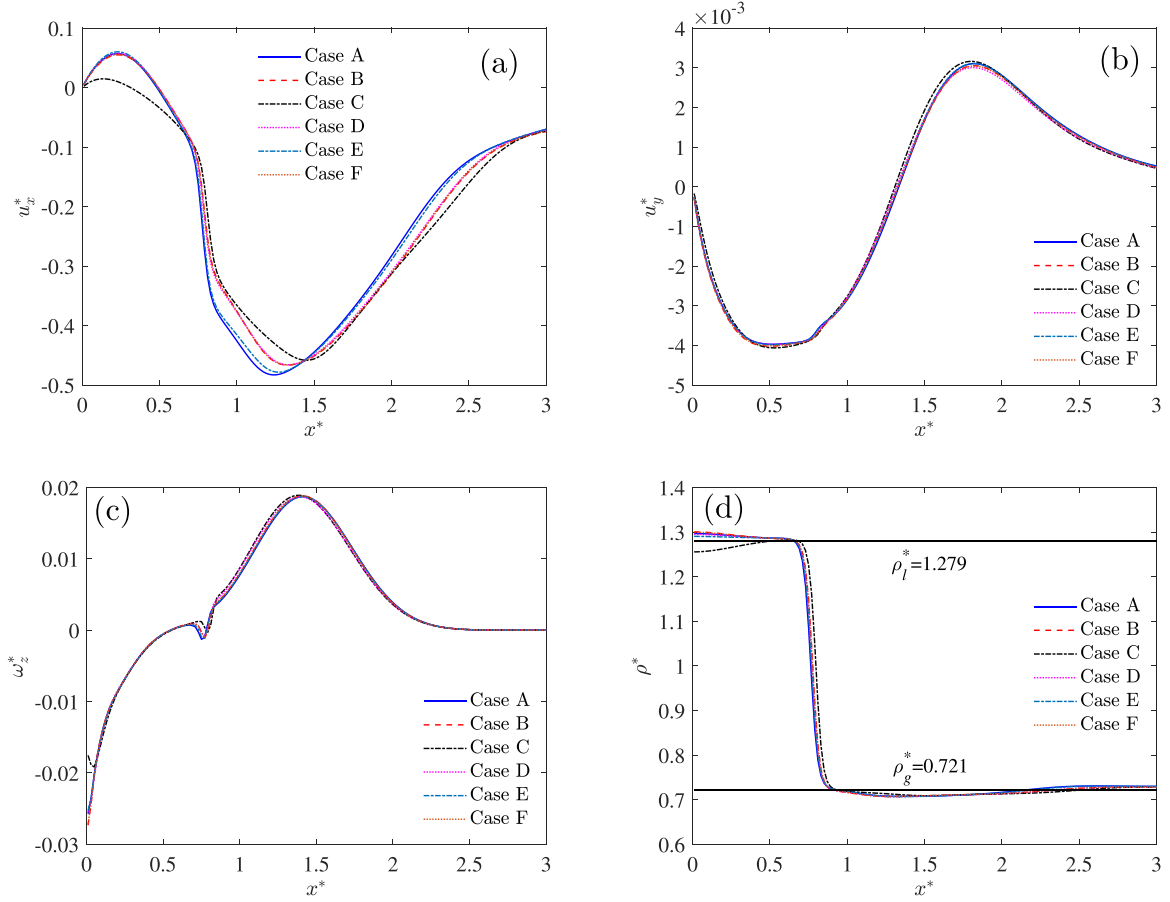


FIG. 9. Comparison of the normalized (a) vertical velocity component $u_x^* \equiv u_x/U$, (b) horizontal velocity component $u_y^* \equiv u_y/U$, (c) vorticity component $\omega_z^* \equiv \omega_z/(U/R)$ and (d) density $\rho^* = \rho/\rho_l$ at $y^* = 4$ along the horizontal direction. $\rho_l \equiv (\rho_l + \rho_g)/2$ is defined as the interfacial density. $We = 85.7$ and $Re = 100$.

where V_m accounts for the attractive molecular interaction and the density gradient. The two coefficients a and κ are given by

$$a = \frac{2}{3}\pi\sigma^3 \frac{\phi_\sigma}{m^2} \frac{\gamma_p}{\gamma_p - 3}, \quad \kappa = \frac{2}{15}\pi\sigma^5 \frac{\phi_\sigma}{m^2} \frac{\gamma_p}{\gamma_p - 5}. \quad (69)$$

We notice that the coefficients in Eq. (69) are the same as those recently reported by Struchtrup and Frezzotti [44] and by Frezzotti *et al.* [43]

The Chapman-Enskog expansion of the Enskog-Vlasov equation shows that the thermodynamic pressure p_0 can be written in an unified form, which reads [28,29]

$$p_0 = \rho RT(1 + b\rho\chi) - a\rho^2, \quad (70)$$

where $b = 2\pi\sigma^3/3m$, and $\chi(\rho)$ is a density-dependent pair correlation function. Two new corrections exist in the pressure when compared to the EOS of the ideal gas. The pressure increment $b\rho^2 RT\chi$ arises due to the short-range molecular interaction dominated by the strong repulsive force, while the pressure reduction $-a\rho^2$ is caused by the long-range attractive molecular interaction. Different choice of $\chi(\rho)$ will lead to different EOS. For example, the vdW EOS can be recovered by choosing $\chi(\rho) = \frac{1}{1-b\rho}$ [28,29]. Similarly, if $\chi(\rho) = \frac{1-b\rho/8}{(1-b\rho/4)^3}$ is used, the Carnahan-Starling (CS) EOS [45] is recovered.

Combining Eqs. (6) and (70), one can obtain a natural decomposition of the chemical potential force as follows:

$$-\rho\nabla\mu_\rho = -\nabla[\rho RT(1 + b\rho\chi)] - \rho\nabla V_m. \quad (71)$$

Equation (71) indicates that the mean field force per unit volume $-\rho\nabla V_m$ only serves as a portion of the chemical potential gradient force. The remaining term $-\nabla[\rho RT(1 + b\rho\chi)]$ originates from the Enskog correction for dense fluids.

However, He and Doolen [28] also reported an expression of the mean field force similar to Eq. (68):

$$\mathbf{F}'_m = -\nabla V'_m, \quad V'_m = -2a'\rho - \kappa'\nabla^2\rho, \quad (72)$$

where the coefficients were given by

$$a' = -\frac{1}{2} \int_{r>\sigma} V(r)dr, \quad \kappa' = -\frac{1}{6} \int_{r>\sigma} r^2 V(r)dr. \quad (73)$$

Then, if the Sutherland potential in Eq. (61) is applied to their model, Eq. (73) will give

$$a' = \frac{2}{\gamma_p} \pi \sigma^3 \frac{\phi_\sigma}{m^2} \frac{\gamma_p}{\gamma_p - 3}, \quad \kappa' = \frac{2}{3\gamma_p} \pi \sigma^5 \frac{\phi_\sigma}{m^2} \frac{\gamma_p}{\gamma_p - 5}. \quad (74)$$

Note that $\gamma_p > 5$ is still required to guarantee the convergence of the integrals in Eq. (73). The corresponding thermodynamic pressure is written as

$$p_0 = \rho RT(1 + b'\rho\chi) - a'\rho^2. \quad (75)$$

By comparing Eq. (69) with Eq. (74), we find that the coefficients reported by Struchtrup and Frezzotti [44] are different from those derived by He and Doolen [28], which are related through

$$a' = (3/\gamma_p)a < a \quad \text{and} \quad \kappa' = (5/\gamma_p)\kappa < \kappa, \quad (76)$$

for fixed parameters σ , m , γ_p (>5), and ϕ_σ . In addition, it is obvious that $b' = b$ due to fixed σ and m . As a result, this difference will yield different EOSs as shown in Eqs. (70) and (75). Take the vdW EOS as an example. Because of the difference between Eqs. (69) and (74), the critical values of Eq. (75) are $\rho'_c = \rho_c$, $T'_c = (3/\gamma_p)T_c$, $p'_c = (3/\gamma_p)p_c$. In other words, the difference of the coefficients a and b leads to a lower critical temperature and critical pressure while the critical density is not changed.

The reason for this difference in the coefficients can be explained as follows. He and Doolen [28] derived their mean field force expression by simplifying the integral \mathcal{G}_2 , which described the long-range attractive interaction in the Bogoliubov-Born-Green-Kirkwood-Yvon (BBGKY) theory. To be consistent with their derivation, we follow the symbols used in their paper for this short discussion, where the two-particle distribution function is $f^{(2)}(\xi_1, \mathbf{r}_1, \xi_2, \mathbf{r}_2) \approx f(\xi_1, \mathbf{r}_1)f(\xi_2, \mathbf{r}_2)$ in the integral domain $\{\mathcal{D}_2 : \|\mathbf{r}_2 - \mathbf{r}_1\| \geq \sigma\}$. Here, \mathbf{r}_1 and \mathbf{r}_2 are the spatial locations of two colliding particles, and ξ_1 and ξ_2 are their corresponding velocities. The integral \mathcal{G}_2 is evaluated as

$$\begin{aligned} \mathcal{G}_2 &= \int_{\mathcal{D}_2} \int \frac{\partial f^{(2)}}{\partial \xi_1} \cdot \nabla_{\mathbf{r}_1} V(r_{12}) d\xi_2 d\mathbf{r}_2 \\ &= \frac{\partial f(\xi_1, \mathbf{r}_1)}{\partial \xi_1} \cdot \int_{\mathcal{D}_2} \int f(\xi_2, \mathbf{r}_2) \nabla_{\mathbf{r}_1} V(r_{12}) d\xi_2 d\mathbf{r}_2 \\ &= \frac{\partial f(\xi_1, \mathbf{r}_1)}{\partial \xi_1} \cdot \int_{\mathcal{D}_2} \left[\int f(\xi_2, \mathbf{r}_2) d\xi_2 \right] \nabla_{\mathbf{r}_1} V(r_{12}) d\mathbf{r}_2 \\ &= \frac{\partial f(\xi_1, \mathbf{r}_1)}{\partial \xi_1} \cdot \int_{\mathcal{D}_2} \rho(\mathbf{r}_2) \nabla_{\mathbf{r}_1} V(r_{12}) d\mathbf{r}_2, \end{aligned} \quad (77)$$

where $\mathbf{r}_{12} = -\mathbf{r}_{21} = \mathbf{r}_1 - \mathbf{r}_2$ and $r_{12} = r_{21} = \|\mathbf{r}_1 - \mathbf{r}_2\|$. By applying the identity

$$\nabla_{\mathbf{r}_1} V(r_{12}) = \frac{dV(r_{12})}{dr_{12}} \frac{\mathbf{r}_1 - \mathbf{r}_2}{r_{12}} \quad (78)$$

to the last equality in Eq. (77), we obtain

$$\mathbf{F}_m(\mathbf{r}_1) = \int_{\mathcal{D}_2} \frac{dV(r_{12})}{dr_{12}} \frac{\mathbf{r}_{21}}{r_{12}} \rho(\mathbf{r}_2) d\mathbf{r}_2. \quad (79)$$

After the substitution $\mathbf{r}_1 \Rightarrow \mathbf{x}$ and $\mathbf{r}_2 \Rightarrow \mathbf{x}_1$, Eq. (79) is consistent with Eq. (62).

Since the integral domain \mathcal{D}_2 is explicitly dependent on \mathbf{r}_1 , the order of $\int_{\mathcal{D}_2}$ and $\nabla_{\mathbf{r}_1}$ cannot be arbitrarily exchanged mathematically. It is noted that He and Doolen [28] exchange the order of $\int_{\mathcal{D}_2}$ and $\nabla_{\mathbf{r}_1}$ (perhaps as a rough estimate), which gives

$$\int_{\mathcal{D}_2} \rho(\mathbf{r}_2) \nabla_{\mathbf{r}_1} V(r_{12}) d\mathbf{r}_2 \rightarrow \nabla_{\mathbf{r}_1} \left[\int_{\mathcal{D}_2} \rho(\mathbf{r}_2) V(r_{12}) d\mathbf{r}_2 \right]. \quad (80)$$

Then, He and Doolen [28] introduce the intermolecular potential as

$$V'_m(\mathbf{r}_1) = \int_{\mathcal{D}_2} \rho(\mathbf{r}_2) V(r_{12}) d\mathbf{r}_2. \quad (81)$$

After the substitution $\mathbf{r}_1 \Rightarrow \mathbf{x}$ and $\mathbf{r}_2 \Rightarrow \mathbf{x}_1$ (recovering the notations in this paper), Eq. (81) is recast to

$$V'_m(\mathbf{x}) = \int_{r>\sigma} \rho(\mathbf{x} + \mathbf{r}) V(r) d\mathbf{r}. \quad (82)$$

Performing the second-order Taylor-series expansion on the density with respect to \mathbf{r} gives

$$\begin{aligned} V'_m(\mathbf{x}) &= \left[\int_{r>\sigma} V(r) d\mathbf{r} \right] \rho(\mathbf{x}) \\ &\quad + \left[\int_{r>\sigma} \frac{1}{2} r_j r_k V(r) d\mathbf{r} \right] \frac{\partial^2 \rho}{\partial x^j \partial x^k}(\mathbf{x}) \\ &= \left[\int_{r>\sigma} V(r) d\mathbf{r} \right] \rho(\mathbf{x}) + \left[\frac{1}{6} \int_{r>\sigma} r^2 V(r) d\mathbf{r} \right] \nabla^2 \rho. \end{aligned} \quad (83)$$

By comparing Eqs. (72) and (83), the coefficients in (73) are obtained.

In summary, the inconsistency between the coefficients provided by He and Doolen [28] and Struchtrup and Frezzotti [44] is caused by the rough estimate introduced in Eq. (80). Despite having this defect in deriving the coefficients, He and Doolen correctly concluded that the long-range molecular interaction could be modeled as a potential force, which was formally consistent with the result in Eq. (68). For practical applications, we have noticed that these two coefficients (a and κ) are generally viewed as adjustable input parameters instead of being evaluated through their definitions at the molecular level. Therefore, the results of these simulations will not be influenced by the inconsistency discussed here.

IX. CONCLUSIONS AND DISCUSSIONS

In this paper, relationships among fundamental physical concepts involved in the diffuse interface modeling are discussed and examined for an isothermal single-component liquid-vapor system.

First, by combining theoretical and numerical methods, a flat surface at equilibrium is discussed as a canonical problem from two different perspectives including chemical equilibrium and force balance. In particular, the Maxwell equal-area rule is naturally recovered as a direct corollary. Although it is geometrically simple, the force structure in the transition region between the two fluids is clearly revealed, which demonstrates that the capillary contributions due to the density gradients can suppress the mechanical instability of the thermodynamic pressure and therefore result in constant hydrodynamic pressure and chemical potential.

Second, for a flat surface at equilibrium, we compare the results obtained from the double-well approximation with three constant coefficients [namely, $\beta(\rho_l)$, $\beta(\rho_g)$, and β_{CH}] and those obtained by using the vdW EOS. We show that applying the double-well approximation to the bulk free

energy density can provide qualitative predictions for relatively high density ratio ($\rho_l/\rho_g = 7.784$) and satisfactory results for relatively low density ratio ($\rho_l/\rho_g = 1.774$).

For $\rho_l/\rho_g = 7.784$, the results are sensitive to the choice of the coefficient β_0 . We observe that the results with both $\beta_0 = \beta(\rho_l)$ and $\beta_0 = \beta_{CH}$ [β_{CH} was derived by Cahn and Hilliard [34] in a small vicinity of the critical point (ρ_c, T_c)] are close to the analytical solutions obtained from the vdW EOS, while those with $\beta_0 = \beta_{CH}$ show larger discrepancies. In contrast, the results with $\beta_0 = \beta(\rho_g)$ exhibit larger differences compared to those using $\beta_0 = \beta(\rho_l)$ and $\beta_0 = \beta_{CH}$. For $\rho_l/\rho_g = 1.774$, the results from $\beta_0 = \beta_{CH}$ are very close to the analytical solution, and show much smaller discrepancies compared to those from $\beta_0 = \beta(\rho_l)$ and $\beta(\rho_g)$. The main cause for this observation is attributed to the nonlinear variation of the generalized coefficient function in the double-well formulation [Eq. (42)] at different density ratios.

Then, in order to validate the applicability of the double-well approximation to complex two-phase hydrodynamics for near-critical fluids, we simulate a droplet impact on a hydrophilic wall by using a recently proposed well-balanced discrete unified gas kinetic scheme (WB-DUGKS). The comparison indicates that the double-well approximation (derived from a flat surface at equilibrium) can provide reliable prediction for two-phase flow in the low-density-ratio limit. The interfacial density structure of the EOS is well retained by the double-well approximation.

Finally, the reason for the inconsistency between the coefficients a and κ in the mean-field force expressions of the existing literature is revealed. Since the coefficients are usually treated as input parameters rather than being evaluated at the molecular level, the inconsistency will not cause confusion in the existing simulations.

The data that support the findings of this study are available from the corresponding author upon reasonable request.

ACKNOWLEDGMENT

Computing resources were provided by the Center for Computational Science and Engineering of Southern University of Science and Technology.

APPENDIX A: CODE VALIDATION

In order to validate the developed WB-DUGKS code, we simulate the classical flat interface problem of Yang *et al.* [24,32] The central difference-based reconstruction scheme (CD-FRS) is used in the evaluation of the kinetic flux across the cell interfaces. The computational domain is $L_y \times L_x = 40 \times 200$ unless otherwise stated. The liquid slab is placed between the locations $x_L = 50$ and $x_H = 150$ with the remaining space filled with vapor. Periodic boundary conditions are employed at the four boundaries. The relaxation time is fixed at $\tau = 0.3$ and the Courant-Friedrichs-Lewy (CFL) number is equal to 0.5. The density field is initialized by

$$\rho(x, y) = \rho_g + \frac{\rho_l - \rho_g}{2} \left[\tanh \frac{2(x - x_L)}{W} - \tanh \frac{2(x - x_H)}{W} \right], \tag{A1}$$

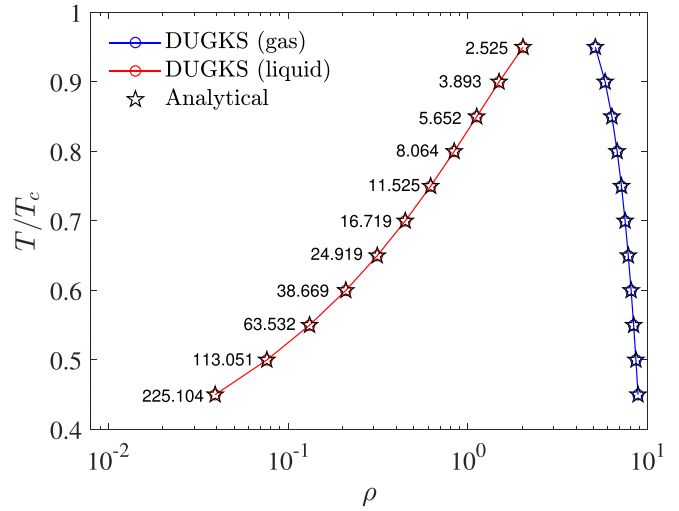


FIG. 10. Comparison of the coexisting densities predicted by the WB-DUGKS and the theoretical values. The density ratios ρ_l/ρ_g are marked for different temperatures.

where $W = 5$ is the interfacial thickness parameter, and ρ_l and ρ_g denote the liquid and vapor densities at saturation, respectively. The vdW EOS is considered with the parameters given as $a = 9/392$, $b = 2/21$, and $R = 1$. The coefficient κ is fixed as 0.02. The normalized temperature T/T_c ranges from 0.45 to 0.95.

When $N_x = 200$ uniform grid points are used in the x direction (namely, $\Delta x = 1$, $N_x = 200$, and $L_x = 200$), the WB-DUGKS always works well for temperature ranging from $T/T_c = 0.95$ (the density ratio $\rho_l/\rho_g = 2.525$) to $T/T_c = 0.55$ ($\rho_l/\rho_g = 63.532$) but fails at lower temperature $T/T_c < 0.55$ due to inaccurate evaluation of the interfacial force in the transition region. The case $T/T_c = 0.5$ (the density ratio $\rho_l/\rho_g = 113.051$) is successfully simulated with $N_x = 400$ uniform points in the x direction (namely, $\Delta x = 0.5$ and $L_x = 200$). It is found that the simulated density ratio could be further increased with higher grid resolution. For example, the case $T/T_c = 0.45$ (the density ratio $\rho_l/\rho_g = 225.104$) can be simulated with $N_x = 800$ and $\Delta x = 0.25$. As shown in Fig. 10, the bulk densities produced by the WB-DUGKS are in excellent agreement with the theoretical values obtained from the solution of $p_0(\rho_l) = p_0(\rho_g)$ and $\mu_0(\rho_l) = \mu_0(\rho_g)$ (or the Maxwell construction rule).

After having the coexisting densities in the bulk regions, the analytical density distribution in the transition region is solved as the solution of Eq. (16) with the conditions $\rho(-\infty) = \rho_g$, $\rho(+\infty) = \rho_l$ and $\rho(0) = (\rho_l + \rho_g)/2$. Figure 11 compares the density profiles produced by the WB-DUGKS and the analytical solution. It is observed that excellent agreements are achieved for different temperatures, which indicates that the interfacial structure in the transition region can be well predicted by the WB-DUGKS. The comparison shown here could be viewed as a supplement to the work of Yang *et al.* [24] where the interfacial structure predicted by the WB-DUGKS was not directly compared with the analytical solution.

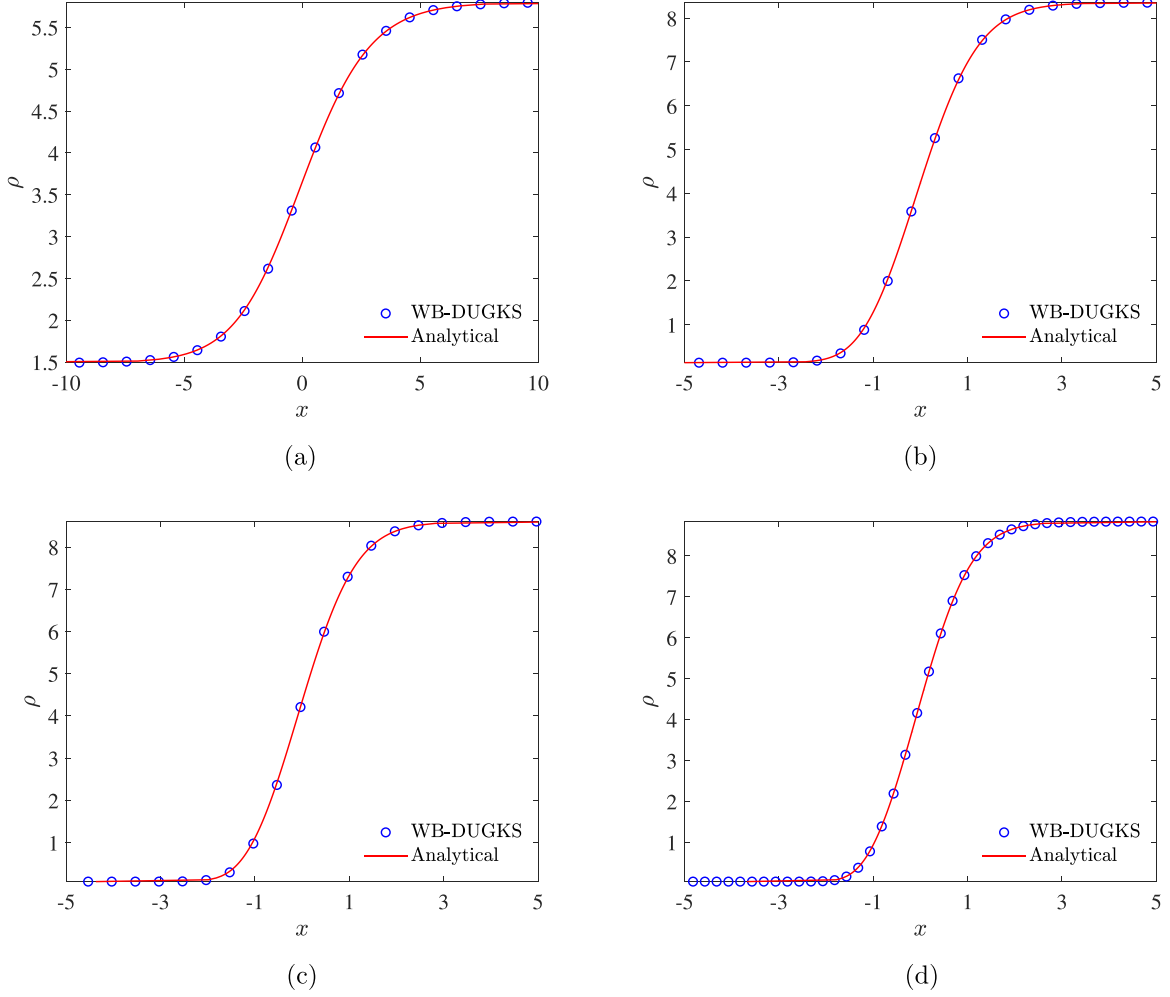


FIG. 11. Comparison of the density profiles produced by the WB-DUGKS and the analytical solution. (a) $T/T_c = 0.9$, $\rho_l/\rho_g = 3.893$. (b) $T/T_c = 0.55$, $\rho_l/\rho_g = 63.532$. (c) $T/T_c = 0.5$, $\rho_l/\rho_g = 113.051$. (d) $T/T_c = 0.45$, $\rho_l/\rho_g = 225.104$.

APPENDIX B: L_2 ERRORS BETWEEN ANALYTICAL AND APPROXIMATE SOLUTIONS

The L_2 error of the density field is usually defined as

$$\epsilon \equiv \sqrt{\frac{\sum_x [\rho_{ap}(x) - \rho_{an}(x)]^2}{\sum_x [\rho_{an}(x)]^2}}, \quad (\text{B1})$$

where $\rho_{an}(x)$ and $\rho_{ap}(x)$ represent the analytical and approximate solutions, respectively. It seems impossible to compute the L_2 errors by using the analytical and approximate solutions obtained from Eq. (16). In order to perform the calculation, the density interval $[\rho_g, \rho_l]$ should be uniformly divided and the obtained solutions take the form $x = x(\rho)$. Even for the same division of $[\rho_g, \rho_l]$, the analytical and approximate solutions will have different nonuniformly distributed x coordinates. Under a given division of the x coordinate in a sufficiently large domain, it is difficult to calculate $\rho = \rho(x)$ from the solution $x = x(\rho)$ without applying some interpolation techniques. Therefore, the L_2 error defined in Eq. (B1) cannot be directly evaluated with the raw data.

As validated in Appendix A, the numerical solution produced by the WB-DUGKS with sufficient grid resolution is in excellent agreement with the analytical solution. Therefore,

the analytical and approximate solutions in Eq. (B1) can be replaced by the corresponding numerical solutions of the WB-DUGKS to calculate the L_2 -errors.

Figure 12(a) shows the L_2 errors of the density between the analytical and approximate solutions at different temperatures. It is found that the L_2 error of the density is almost linearly dependent on the normalized temperature T/T_c between 0.55 and 0.95. The L_2 error of the density with $\beta_0 = \beta(\rho_l)$ is always lower than that with $\beta_0 = \beta(\rho_g)$ under the same temperature. The maximum L_2 error is about 3% for $\beta_0 = \beta(\rho_g)$ and 0.5% for $\beta_0 = \beta(\rho_l)$. It should be noticed that although the global L_2 error is not remarkable for the density distribution, the double-well approximation will greatly influence the distributions of the bulk free energy density $\bar{\psi}$, the thermodynamic pressure \bar{p}_0 , and the capillary stress $-\kappa\rho(d^2\rho/dx^2)$ inside the interfacial region for relatively lower temperatures, which results in the L_2 errors displayed in Figs. 12(b), 12(c), and 12(d). These comparisons suggest that (i) the double-well approximation with $\beta_0 = \beta(\rho_l)$ can always provide better prediction than $\beta_0 = \beta(\rho_g)$, and (ii) the double-well approximation is only suitable for the near-critical fluids with low density ratio whose interfacial structure is not significantly changed by the approximation.

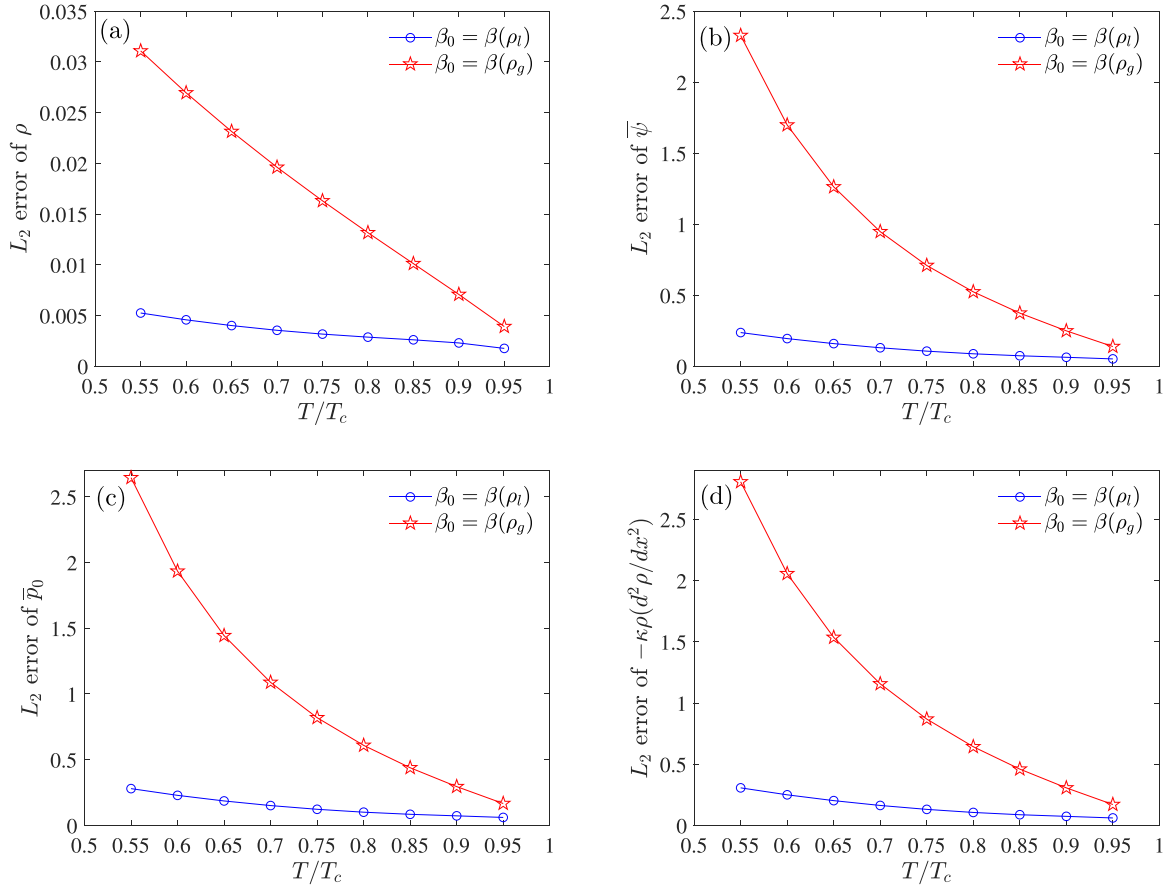


FIG. 12. The L_2 errors of (a) the density ρ , (b) the bulk free energy density $\bar{\psi}$, (c) the thermodynamic pressure \bar{p}_0 , and (d) the capillary stress $-\kappa\rho(d^2\rho/dx^2)$.

APPENDIX C: ON THE SPEED OF SOUND AND INTERFACIAL COMPRESSIBILITY

For the double-well approximation with a constant coefficient β_0 , Eq. (46) shows that the ratio of the sound speeds in the liquid and vapor phases is $c_s(\rho_l)/c_s(\rho_g) = \sqrt{\rho_l/\rho_g}$. Figure 13 displays the ratio of the sound speeds for the vdW EOS and the double-well approximation at different temperatures. It is observed that the ratio of the sound speeds produced by the double-well approximation is always higher than that of the vdW EOS at a given temperature. The difference gradually becomes prominent as the temperature decreases below the critical temperature. For near-critical fluids with low density ratio, the ratios of the sound speeds are very close to each other. Therefore, the double-well approximation not only influences the density structure in the interfacial region but also modifies the sound speeds in the bulk phases. Despite all these changes, the double-well approximation can realize effective phase separation even for high-density-ratio fluids without guaranteeing the maintenance of the original interfacial structure [17,31,39,46].

For the isothermal two-phase fluid system, the weak compressibility (characterized by the velocity divergence) mainly concentrates inside the interfacial layer, which is basically proportional to the Laplacian of the chemical potential (namely, the divergence of the chemical potential gradient).

In the bulk regions, the density variation is small, the chemical potential is close to a constant, and the compressibility can be neglected. It is worth mentioning that the slope

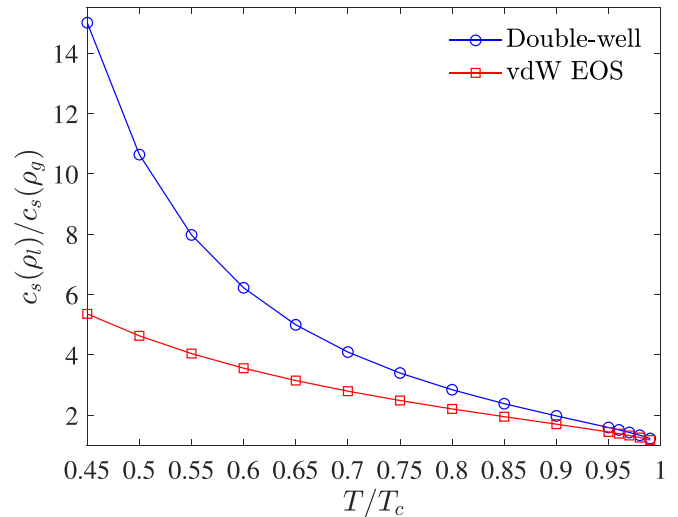


FIG. 13. Comparison of the ratio of the sound speeds in bulk phases $c_s(\rho_l)/c_s(\rho_g)$ with respect to the normalized temperature T/T_c .

$\partial_\rho p_0$ could become negative in the interfacial region, which is mechanically unstable. According to the existing studies [47,48], the coupling between the negative slope and the weak

compressibility could cause pressure variation and trigger isothermal evaporation and condensation in the interfacial region.

-
- [1] J. D. van der Waals, The thermodynamic theory of capillarity under the hypothesis of a continuous variation of density, *J. Stat. Phys.* **20**, 200 (1979).
- [2] M. R. Swift, W. R. Osborn, and J. M. Yeomans, Lattice Boltzmann Simulation of Nonideal Fluids, *Phys. Rev. Lett.* **75**, 830 (1995).
- [3] A. Prosperetti and G. Tryggvason, *Computational Methods for Multiphase Flow* (Cambridge University Press, Cambridge, 2007).
- [4] D. M. Anderson, G. B. McFadden, and A. A. Wheeler, Diffuse-interface methods in fluid mechanics, *Annu. Rev. Fluid Mech.* **30**, 139 (1998).
- [5] J. A. Sethian and S. Peter, Level set methods for fluid mechanics, *Annu. Rev. Fluid Mech.* **35**, 341 (2003).
- [6] D. Jacqmin, Calculation of two-phase Navier-Stokes flows using phase-field modeling, *J. Comput. Phys.* **155**, 96 (1999).
- [7] D. Jamet, O. Lebaigue, N. Coutris, and J. M. Delhay, The second gradient theory: A tool for the direct numerical simulation of liquid-vapor flows with phase-change, *Nucl. Eng. Des.* **204**, 155 (2001).
- [8] Z. L. Guo and C. Shu, *Lattice Boltzmann Method and Its Applications in Engineering* (World Scientific, Singapore, 2013).
- [9] X. Shan and H. Chen, Lattice Boltzmann model for simulating flows with multiple phases and components, *Phys. Rev. E* **47**, 1815 (1993).
- [10] Z. Guo, Well-balanced lattice Boltzmann model for two-phase systems, *Phys. Fluids* **33**, 031709 (2021).
- [11] Y. Wang, H. Liu, and H. Yuan, Recent advances in theory, simulations, and experiments on multiphase flows, *Phys. Fluids* **34**, 040401 (2022).
- [12] S. Benzoni-Gavage, S. Descombes, D. Jamet, and L. Mazet, Structure of Korteweg models and stability of diffuse interfaces, *Interface Free Bound.* **7**, 371 (2005).
- [13] Q. Li, K. H. Luo, Y. J. Gao, and Y. L. He, Additional interfacial force in lattice Boltzmann models for incompressible multiphase flows, *Phys. Rev. E* **85**, 026704 (2012).
- [14] B. Wen, X. Zhou, B. He, C. Zhang, and H. Fang, Chemical-potential-based lattice Boltzmann method for nonideal fluids, *Phys. Rev. E* **95**, 063305 (2017).
- [15] C. Zhang, K. Yang, and Z. Guo, A discrete unified gas-kinetic scheme for immiscible two-phase flows, *Int. J. Heat Mass Transf.* **126**, 1326 (2018).
- [16] T. Chen, C. Victor, Z. Guo, J. C. Brändle de Motta, and L.-P. Wang, Simulation of immiscible two-phase flows based on a kinetic diffuse interface approach, in 10th International Conference on Multiphase Flow, ICMF 2019, Rio de Janeiro, Brazil, May 19–24, 2019 (unpublished).
- [17] H. Liang, H. Liu, Z. Chai, and B. Shi, Lattice Boltzmann method for contact-line motion of binary fluids with high density ratio, *Phys. Rev. E* **99**, 063306 (2019).
- [18] E. Dinesh Kumar, S. A. Sannasiraj, and V. Sundar, Phase field lattice Boltzmann model for air-water two phase flows, *Phys. Fluids* **31**, 072103 (2019).
- [19] L. Zheng, S. Zheng, and Q. Zhai, Eliminating spurious currents in phase-field theory-based lattice Boltzmann equation for two-phase flows, *Phys. Fluids* **33**, 092102 (2021).
- [20] R. Huang, H. Wu, and N. A. Adams, Mesoscopic Lattice Boltzmann Modeling of the Liquid-Vapor Phase Transition, *Phys. Rev. Lett.* **126**, 244501 (2021).
- [21] X. Li, Z.-Q. Dong, Y. Li, L.-P. Wang, X.-D. Niu, H. Yamaguchi, D.-C. Li, and P. Yu, A fractional-step lattice Boltzmann method for multiphase flows with complex interfacial behavior and large density contrast, *Int. J. Multiphase Flow* **149**, 103982 (2022).
- [22] Y.-D. Zhang, A.-G. Xu, J.-J. Qiu, H.-T. Wei, and Z.-H. Wei, Kinetic modeling of multiphase flow based on simplified Enskog equation, *Front. Phys.* **15**, 62503 (2020).
- [23] W. Zeng, C. Zhang, and Z. Guo, Well-balanced discrete unified gas-kinetic scheme for two-phase systems, *Phys. Fluids* **34**, 052111 (2022).
- [24] Z. Yang, S. Liu, C. Zhuo, and C. Zhong, Free-energy-based discrete unified gas kinetic scheme for van der waals fluid, *Entropy* **24**, 1202 (2022).
- [25] G. S. Rowlinson and B. Widom, *Molecular Theory of Capillarity* (Clarendon, Oxford, 1982).
- [26] C. Zhang, Z. Guo, and H. Liang, On the formulations of interfacial force in the phase-field-based lattice Boltzmann method, *Int. J. Numer. Methods Fluids* **93**, 2225 (2021).
- [27] T. Lee and P. F. Fischer, Eliminating parasitic currents in the lattice Boltzmann equation method for nonideal gases, *Phys. Rev. E* **74**, 046709 (2006).
- [28] X. He and G. D. Doolen, Thermodynamic foundations of kinetic theory and lattice boltzmann models for multiphase flows, *J. Stat. Phys.* **107**, 309 (2002).
- [29] S. Chapman and T. G. Cowling, *The Mathematical Theory of Non-uniform Gases* (Cambridge University, Cambridge, 1970).
- [30] A. A. Vlasov, The vibrational properties of an electron gas, *Sov. Phys. Usp.* **10**, 721 (1968).
- [31] T. Lee and C.-L. Lin, A stable discretization of the lattice Boltzmann equation for simulation of incompressible two-phase flows at high density ratio, *J. Comput. Phys.* **206**, 16 (2005).
- [32] Z. Yang, S. Liu, C. Zhuo, and C. Zhong, Pseudopotential-based discrete unified gas kinetic scheme for modeling multiphase fluid flows, *Adv. Aerodyn.* **4**, 32 (2022).
- [33] L. Zheng, T. Lee, Z. Guo, and D. Rumschitzki, Shrinkage of bubbles and drops in the lattice Boltzmann equation method for nonideal gases, *Phys. Rev. E* **89**, 033302 (2014).
- [34] J. W. Cahn and J. E. Hilliard, Free energy of a nonuniform system. I. Interfacial free energy, *J. Chem. Phys.* **28**, 258 (1958).
- [35] Y. Q. Zu and S. He, Phase-field-based lattice Boltzmann model for incompressible binary fluid systems with density and viscosity contrasts, *Phys. Rev. E* **87**, 043301 (2013).
- [36] S. M. Allen and J. W. Cahn, Mechanisms of phase transformations within the miscibility gap of Fe-rich Fe-Al alloys, *Acta Metall.* **24**, 425 (1976).

- [37] X. W. Shan, X.-F. Yuan, and H. Chen, Kinetic theory representation of hydrodynamics: A way beyond the Navier-Stokes equation, *J. Fluid Mech.* **550**, 413 (2006).
- [38] H. Ding and P. D. M. Spelt, Wetting condition in diffuse interface simulations of contact line motion, *Phys. Rev. E* **75**, 046708 (2007).
- [39] Z. Yang, Conservative multilevel discrete unified gas kinetic scheme for modeling multiphase flows with large density ratios, *Phys. Fluids* **34**, 043316 (2022).
- [40] L. De Sobrino, On the kinetic theory of a van der Waals gas, *Can. J. Phys.* **45**, 363 (1967).
- [41] M. Grmela, Kinetic equation approach to phase transitions, *J. Stat. Phys.* **3**, 347 (1971).
- [42] J. Karkheck and G. Stell, Kinetic mean-field theories, *J. Stat. Phys.* **75**, 1475 (1981).
- [43] A. Frezzotti, L. Gibelli, and S. Lorenzani, Mean field kinetic theory description of evaporation of a fluid into vacuum, *Phys. Fluids* **17**, 012102 (2005).
- [44] H. Struchtrup and A. Frezzotti, in *31st International Symposium on Rarefied Gas Dynamics: RGD31, Grad's 13 moments approximation for Enskog-Vlasov equation, 23–27 July 2018, Glasgow*, edited by Y. Zhang, D. R. Emerson, D. Lockerby, and L. Wu, AIP Conf. Proc. No. 2132 (AIP, New York, 2019), p. 120007.
- [45] N. F. Carnahan and K. E. Starling, Equation of state for nonattracting rigid spheres, *J. Chem. Phys.* **51**, 635 (1969).
- [46] J. Lowengrub and L. Truskinovsky, Quasi-incompressible Cahn-Hilliard fluids and topological transitions, *Proc. R. Soc. London A* **454**, 2617 (1998).
- [47] T. Lee and C.-L. Lin, Pressure evolution lattice-Boltzmann-equation method for two-phase flow with phase change, *Phys. Rev. E* **67**, 056703 (2003).
- [48] L. Baroudi and T. Lee, Effect of interfacial mass transport on inertial spreading of liquid droplets, *Phys. Fluids* **32**, 032101 (2020).